Characterization and Analysis of Continuous Wave Terahertz Photomixers

by

Mehrnoosh Khabiri

A thesis
presented to the University of Waterloo
in fulfillment of the
thesis requirement for the degree of
Master of Applied Science
in
Electrical and Computer Engineering

Waterloo, Ontario, Canada, 2012

AUTHOR'S DECLARATION

I hereby declare that I am the sole author of this thesis. This is a true copy of the thesis, including any required final revisions, as accepted by my examiners.

I understand that my thesis may be made electronically available to the public.

Abstract

In recent years, *Terahertz* (THz) technology has become a very active field of research in regards to its wide range of potential applications such as biosensing, biomedical imaging, pharmaceutical, security, and many others. There are different methods to generate THz radiation. Photomixing is one of the *Continuous Wave* (CW) THz generation methods in which the output of two single-mode lasers or the output of a dual-mode laser with different center frequencies are combined in a nonlinear medium such as photoconductors or superconductors. The photomixing system is designed such that the difference of the laser frequencies falls in the THz range. The generated THz wave can be coupled to an integrated antenna or waveguide. The CW THz photomixer sources are potentially compact, low cost, low power consuming, coherent, and highly tunable. However, the primary disadvantage of using photomixers is that the output power is relatively low compared with other THz sources.

Photomixer modeling requires solving both semiconductor and electromagnetic problems. In contrast to most of the researches which only report either experimental results or simple analytical model to characterize the photomixers, in this research, a computational simulation method is presented to analyze and model the photomixer devices. The proposed computational method combines a semiconductor solver and a full-wave electromagnetic simulator to rigorously analyze and optimize an integrated THz photomixer antenna device. In this method, by solving Maxwell's equations and then the drift-diffusion charge carrier transport model, the generated THz photo-current inside the photomixer device is obtained. This THz photo-current is modeled as a current source in the antenna feed to find the radiated THz power. Using the proposed simulation method the effects of photomixer parameters on the THz photo-current and radiated power is accurately investigated and the results of a parametric study on various parameters such as carrier lifetime of material, incident optical power density, applied bias voltage, the THz beat frequency, and the gap size are presented.

Acknowledgements

I would like to express my sincere gratitude to my supervisor, Professor Safieddin Safavi-Naeini for his invaluable guidance, encouragement, and support. I really appreciate his endless kindness, patience, and help during my graduate study.

I also would like to thank Dr. Mohammad Neshat for his valuable directions and discussions during the course of this research.

I express my thanks to Dr. Daryoosh Saeedkia, Dr. Arash Rohani and Dr. Mohammadreza Esmaeili from THz lab for their help.

Last but not least, special thanks to my dear family for their nonstop love and support. I am incredibly grateful for my wonderful family.

This research was supported by National Science and Engineering Research Council (NSERC) of Canada and Research In Motion (RIM).

Dedication

To my dear parents for their unconditional love and sacrifice, and

To love of my life, Mehrbod, for his endless love and support

Table of Contents

List of Figures

List of Tables

Chapter 1
Introduction

1.1 Why THz?

The THz gap lies between the microwave and infrared regions of the electromagnetic spectrum which is roughly in the frequency range of 300 GHz to 10 THz. In recent years, THz generation and detection has drawn a lot of attention due to its new applications in many fields such as biosensing [1], biomedical imaging [2], pharmaceutical [3, 4], security [5], high-speed wireless communication [6], and radio astronomy [7, 8]. The THz frequency range has shown some unique properties which makes THz systems a promising tool for real world applications. These properties can be listed as follows:

- THz radiation can penetrate many materials such as paper, soil, fabric, plastic, and wood. Therefore it can be used for detecting hidden objects [35] such as weapons, explosive materials, and illegal drugs inside mail, luggage, and persons.
- THz radiation is non-ionizing and therefore is safer than comparable technologies such as X-rays for medical imaging. THz medical imaging has been applied for diagnosing the diseases like skin cancer [9], and other cancer tissues, and identifying dental caries [10]. Another application of THz systems is in the pharmaceutical industry [3, 4] because of its nondestructive effect on drugs.
- Many substances have a signature frequency "fingerprint" in the THz range of the electromagnetic spectrum [32-34]. Hence, it is possible to distinguish different ingredients and materials because of their absorption and reflection features in the THz range. THz spectroscopy has also been used to study the characteristic spectra of pharmaceutical products and explosive materials.

Despite the significant advantages of THz technology, the greatest limitation in the modern THz systems is the lack of a compact, high power, low cost, portable, room temperature THz source [21, 42].

1.2 Motivation and Objective

In recent years, the generation and detection of THz radiation has attracted a lot of interest because of its potential applications in many fields. The development of the generation and detection of THz

radiation has already shown great improvement. In addition, further research promises further advancement in both THz applications and technology. Using CW THz systems for imaging and spectroscopy applications have some advantages over the conventional pulsed THz systems. In CW THz radiation, the narrow bandwidth gives a very high spectral density allowing for improved frequency resolution and faster scanning times in imaging and spectroscopy systems [36]. The heterodyne conversion or photomixing is one of the techniques to provide CW THz sources. The advantage of photomixing is the wide tunability of the output THz frequency which is determined by the frequency difference of two CW laser beams. On the other hand, the disadvantage of this technique is a low optical-to-THz conversion efficiency which is defined by ratio of the THz output power to the input optical power. The photomixer device is usually integrated with electrodes and a coupled antenna. The design of the CW THz source by photomixing depends on various parts including the photoconductor materials, the integrated electrodes, the photoconductive gap, and the antenna. By considering the role of each part and their interconnection in an equivalent electrical circuit, an efficient photomixer device can be designed. Therefore, optimizing the photomixer device design to improve the THz output power involves optimizing the material properties, the optical coupling, and the antenna/feed circuit design. The photomixer source impedance is usually high and in the order of 10kΩ [11]. This causes the mismatching problem between the photomixer and the antenna, and affects the radiated THz power. Hence, the impedance matching is one of the important issues to deal with to improve the photomixer performance.

The main goal of this thesis is to study the source excitation of the photoconductive antenna integrated in the photomixer device. The photomixer source modeling is a multifaceted problem consisting of both semiconductor and electromagnetic aspects. Most of the researches characterize the photomixer performance either through the experimental results or simple analytical models rather than a rigorous computational model. This research mainly contributes in: 1) developing the computational simulation methodology to rigorously solve both semiconductor and electromagnetic problems for photomixers, 2) modeling the integrated THz photomixer antenna source to obtain the generated THz photo-current and the radiated THz power, and 3) characterizing the photmixer performance by performing a parametric analysis on various parameters such as carrier lifetime of material, applied optical power density, applied bias voltage, the operating frequency, and the gap size.

1.3 Thesis Overview

This research is organized as follows. A brief review of CW THz photomixer sources with particular emphasis on photomixing theory and concept as well as important factors in the photomixer performance are presented in Chapter 2.

Chapter 3 will discuss the basic semiconductor equations and the drift-diffusion carrier transport model which will be used to obtain the generated THz photo-current inside the photoconductive layer of photomixer device.

In Chapter 4, a computational simulation method is presented to combine a semiconductor solver, such as TCAD Sentaurus, and a full-wave electromagnetic simulator, such as *High Frequency Structure Simulator* (HFSS), to rigorously model an integrated THz photomixer antenna source. The TCAD Sentaurus software [40] is employed to solve the basic semiconductor equations and to obtain the generated THz photo-current inside the photoconductor layer of photomixer. The THz photo-current is used as a current source at the antenna feed, and the antenna simulations and input impedance calculations will be performed by HFSS. In the end, the parameter analysis performed to characterize the photomixer source will be discussed.

Finally, Chapter 5 concludes this research and suggests the future directions.

Chapter 2
THz Generation by Photomixing

In this chapter, the review of photomixing is presented, and the theory and concept behind CW THz photomixer devices is explained. The equivalent circuit of the photomixer device and the THz output power calculation is also presented. Finally, different factors that have an important affect on the performance of photomixer devices are introduced, and the impact of each factor is discussed in detail.

2.1 Introduction

There are various techniques for generating CW THz radiation. These CW THz sources can be categorized as electron beam sources, optically pumped far-infrared gas lasers, solid-state sources, frequency multipliers, THz semiconductor lasers, THz parametric sources, and THz photomixers [12]. Among the investigated methods, photomixing has been a well known method for many years. Photomixers have been proposed as compact, low cost, low power consuming, coherent, and highly tunable CW THz sources [21, 42]. A key advantage of photomixing over other THz sources is the frequency tunability. A significant disadvantage of this method is that the output power is low in comparison with other methods. The typical optical-to-THz conversion efficiency of the photomixer is quiet low bieng 10^{-6}-10^{-5} in the frequency range of 1THz to 3THz [13].

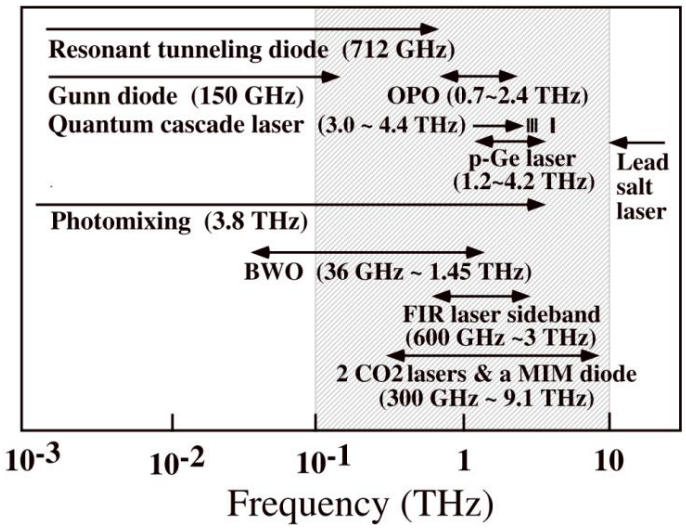

Figure 2.1 The state-of-the-art performance of different conventional coherent tunable THz sources.

The state-of-the-art performance of some conventional coherent tunable THz sources is shown in Figure 2.1 [13]. As it can be seen, the photomixer has a low output power level in the THz frequency.

As a brief review, the photomixing technique was originally proposed almost four decades ago for generating coherent radiation in the microwave region. In the early 1990s, nearly a decade after the first demonstration of the photoconductive generation of pulsed THz radiation, a photomixer design for generating CW THz wave was reported by Brown's group at MIT in 1993 [14]. The same group demonstrated a photomixer device which achieved a reasonable amount of THz power in 1995 [15]. After that, in 1997, Matsuura et al. presented a simpler photomixer design based on low cost lasers [16]. However, the detection methods in those cases were based on a silicon composite bolometer in which, the outputs could only be measured when beyond 3THz [17]. For the first time in 1998, Verghese et al. proposed homodyne detection with antenna-coupled photomixers which are capable of measuring from 25 GHz to 2 THz [18]. After these pioneer works, further researching has opened up the doors to improve the THz source performance and to implement THz technology for different applications.

2.2 Overview of Photomixing technique

Photomixing, also known as optical heterodyne conversion, is a method of generating CW THz radiation in which, the outputs of two single mode lasers or the output of a dual mode laser, with different center frequencies are combined in a nonlinear medium such as a photoconductor or superconductor. The system is designed such that the difference of the laser frequencies falls in the THz range [19]. The generated THz wave can be coupled to an integrated antenna or waveguide.

The integrated THz photomixer antenna devices are one of the best developed photomixers. An integrated THz photomixer antenna device consists of an antenna structure connected to metallic electrodes and is fabricated on ultrafast photoconductive materials. In an integrated THz photomixer antenna, laser beams are focused on a small photoconductive gap which is the feed point of the antenna. A DC bias voltage is also applied to the gap through integrated electrodes. Figure 2.2 shows a schematic diagram of a typical CW THz photomixer device [20].

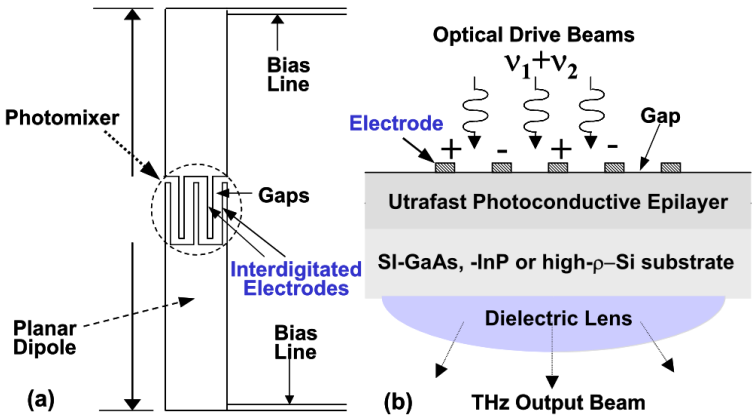

Figure 2.2 (a) The top view of a typical integrated THz photomixer antenna source
(b) The cross-sectional view of the photomixer showing THz radiation
coupling through a dielectric lens to free space.

As it can be seen in Figure 2.2, the two laser beams illuminate the device. The external bias is applied to the integrated electrodes in the feed point of the antenna. The optical beat generates the electron and hole carriers in the photoconductor. When the carrier lifetime of the photoconductor is short enough, the carrier density and thus the current is modulated according to the intensity of the optical beat. The generated THz photo-current acts as the exciting source at the antenna feed point and the coupled antenna will radiate the THz wave into the free space.

The equivalent circuit of the photomixer is shown in Figure 2.3 [21]

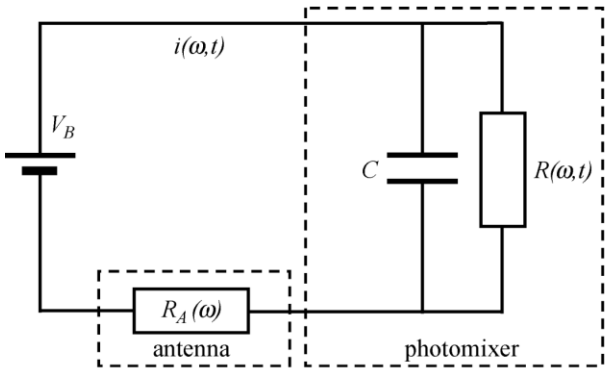

Figure 2.3 The equivalent circuit diagram for the photomixer and antenna.

Let's assume that the laser beams have an average power of P_1 and P_2 with angular frequencies of ω_1 and ω_2 respectively. The input optical power is given by [22]:

$$P_i = P_1 + P_2 + \sqrt{mP_1P_2}\cos(\Delta\omega t - \varphi) \tag{2.1}$$

where $\Delta\omega$ is the difference of the angular frequencies, φ is the phase difference of the optical beams, and m is the mixing efficiency. The mixing efficiency changes from 0 to 1 depending on the spatial overlap of the laser beams [14].

Based on the equivalent circuit shown in Figure 2.3, the total impedance of the circuit is given by:

$$Z(\Delta\omega, t) = R_A + [G(\Delta\omega, t) + j\Delta\omega C]^{-1} \tag{2.2}$$

where the R_A is the antenna resistance, G is the time-dependent conductance modulated at the angular frequency $\Delta\omega$, and C is the capacitance of the photoconductive gap.

Then, the power delivered to the antenna can be obtained by:

$$P(\Delta\omega, t) = R_A \left[\frac{V_B}{Z(\Delta\omega,t)}\right]^2 \tag{2.3}$$

where V_B is the applied bias voltage.

Finally, the THz output power can be derived by the expression below [14]:

$$P_{THz}(\Delta\omega) = \frac{2R_A V_B^2 m P_1 P_2}{A}\left[\frac{\eta\mu e\tau}{rh\nu}\right]^2 \frac{1}{[1+(\Delta\omega\tau)^2][1+(\Delta\omega R_A C)^2]} \tag{2.4}$$

where A is the active area, η is the external quantum efficiency, μ is the carrier mobility, e is the electron change, r is the gap width, $h\nu$ is the photon energy of an optical laser beam, and τ is the carrier recombination lifetime.

When the laser beams have a perfect overlap ($m=1$) and $P_1=P_2$, the THz output power can be reached to its maximum value.

As it can be seen in the equation (2.4), the THz output power is limited by the external quantum efficiency of the photomixer, the photocarrier recombination time, the RC roll-off, and the thermal effects.

2.3 Photomixing Technology Improvement

In this section some key factors to improve the performance of the integrated THz photomixer antenna sources are discussed. The THz output power is limited by some elements. Currently, the level of power is not sufficient for some practical applications. Therefore, there is still much more room for improving the THz output power by optimizing and analyzing the device design.

2.3.1 Substrate Properties

The most important properties for the photoconductive materials used in photomixer devices are:

- Short carrier life time
- High carrier mobility
- Large electrical field break-down

The first and the second required properties are usually difficult to achieve simultaneously.

The LTG-GaAs and ErAs-GaAs are materials that satisfy the mentioned properties and have shown successful development in photomixer devices [20]. The very first time, the LTG-GaAs were used for photomixing was in 1992[14]. The LTG-GaAs were grown on a semi-insulating GaAs substrate using a molecular-beam epitaxy at around 200-300°C so that good crystallinity was maintained while incorporating approximately 1% more arsenic than gallium. After this chemical reaction, the carrier lifetime of the LTG-GaAs could be reduced in the range of 150fs to a few ps [25] which is very short. However, the mobility and field break-down obtained are very low. Annealing at temperatures around 500-600°C causes much of the excess to modify into nm-scale precipitation. Therefore the carrier lifetime stays short enough, but the carrier mobility and material electrical break-down will have increased. Annealed LTG-GaAs have unique properties such as a short carrier life time (around 0.5 ps), relatively good carrier mobility (around 200 cm^2/Vs) and a large break-down field threshold [23]. The field break-down of the LTG-GaAs is typically in the range of 500 kV/cm [25]. The highest field break-down, reported by E. Brown, is up to 1000 kV/cm [20]. These properties of the LTG-GaAs make it the most common photoconductor which has been considered in photomixer devices. A disadvantage of the LTG-GaAs is the difficulty in controlling the growth temperature of it [20]. An alternative material for solving this problem is the ErAs:GaAs. A photomixer device was developed with the growth of ErAs layers embedded in GaAs [24]. ErAs is a semi metallic material and has a rock salt lattice. The lattice constant is approximately same as the GaAs. In a typical photomixer device material, ErAs with a thickness of around one monolayer is deposited during the growth of the GaAs. The ErAs layers in the photomixer material provide efficient recombination, and generated carriers can be captured in the ErAs layers. The ErAs:GaAs has a higher carrier mobility than the LTG-GaAs and its carrier lifetime depends on the time required for excess electron and hole to diffuse to the ErAs nanoparticles [20].

In recent years, the 1550nm based photomixers attracted attention because of the fast development of the telecom frequency. The standard material for this operating frequency is an InGaAs grown lattice matched on InP. At that operating frequency the cost is cheaper than the optical elements. In addition, the photon energy of the LTG-GaAs at 1550nm is roughly half of that at 800nm. Therefore the responsivity of the devices increases two times, and accordingly, the optical-to-THz conversion efficiency enhances four times. The difficulty of this material is that growing InGaAs at low temperatures does not give a short recombination time [25].

2.3.2 Photomixer Antenna

The performance of the antenna is a critical factor in the photomixer's response and efficiency. In the equation (2.4), it has been shown that the THz output power of a photomixer in the small signal limit is proportional to the antenna impedance. The impedance of a planar antenna on LTG-GaAs is at most, a few 100 Ω and much lower than the LTG-GaAs photomixer impedance which is in order of 10 kΩ [22]. Hence, the significant difference between the antenna impedance and the photomixer impedance leads to the impedance mismatching problem, and therefore the THz power delivered to the antenna will decrease as a result. At the early phase of the photomixer device's development, a broadband self-complementary antenna, such as a log-spiral, a log-periodic, and a bow-tie antenna have been used to create frequency independent impedance over a wide range of bandwidth [15, 26] but the impedance of the broadband antenna is typically 70Ω-90Ω which is relatively low. Therefore to improve the THz output power, high impedance antennas were designed. However the bandwidth was limited in that case.

The resonant antenna such as a dipole and slot antenna which have high impedance at the resonant frequency have been used in photomixer devices. The following reasons show how using the resonant antennas will improve the THz output power. First, as mentioned before, the THz output power is limited to the RC time constant roll-off. If the antenna operates a little away from its resonant frequency, its inductance may cancel out the capacitance of the photomixer Therefore, the RC time constant roll-off can be avoided. The second reason is that even when the operation frequency of the antenna is a way from its resonant frequency, the resistance of the antenna can be high enough to provide a higher THz output power compared with the broadband antenna [20].

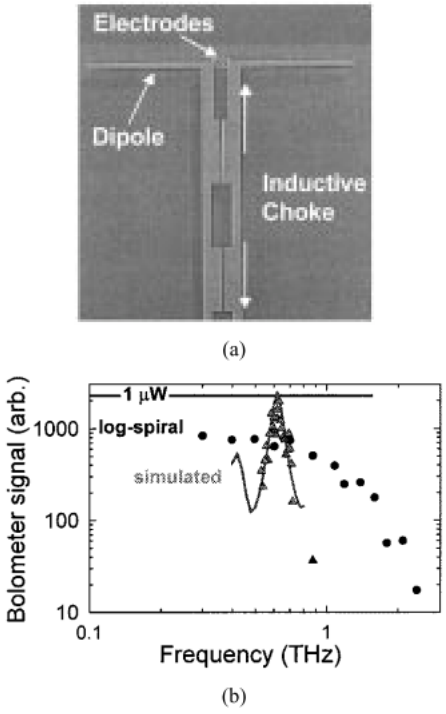

Figure 2.4 (a) A full-wave dipole photomixer device
(b) The output power spectrum of the measured (triangles) and calculated (solid line) results , and the measured log-spiral photomixer device (circles)[27].

Figure 2.4 shows the THz output power characterization of a full wavelength dipole antenna and a log-spiral antenna. As it can be seen in Figure2.4.b, the THz output power of a full wavelength dipole antenna at the resonance frequency improved 2-3 times compared to the log-spiral antenna.

Photomixing with a resonant dual dipole antenna has been investigated by different groups. Using a dual dipole antenna in the photomixer device has some advantages compared to a single dipole antenna. The first advantage is that its radiation pattern is symmetric near the Gaussian beam pattern while a single dipole antenna has relatively large side-robes [27]. Another advantage is the flexibility in the circuit design for tuning at higher frequencies. The dual dipole antenna and the photoconductive gap are connected with a coplanar strip transmission line. The capacitance of the photoconductive gap can be cancelled out by adjusting the length of the transmission line. This property helps for designing at high frequencies.

2.3.3 Thermal Effect

The photomixer performance is limited by the thermal effect. The important sources of heat are the optical power absorption and the Joule heating from the photo-current flowing in a bias field [20].

The radiated THz output power is proportional to the total input power. In fact, a higher input power gives a higher THz output power. The important point is that the maximum laser power on the photoconductive gap is restricted by the thermal damage threshold of the photoconductor. The thermal damage threshold of a small photoconductive gap for LTG-GaAs it is 1 $mW/\mu m^2$, which is approximately 100mW for a $100\mu m^2$ photoconductive gap [26].

The thermal damage threshold is proportional to the substrate thermal conductivity. Therefore substrates with a high thermal conductivity help improve the thermal damage threshold. Some efforts have been done to increase the thermal damage threshold by changing and modifying the substrate material. Silicon has high thermal conductivity which is three times more of the GaAs one. It has been shown that the THz output power of a LTG-GaAs on Si substrate is approximately two times higher than the THz output power of LTG-GaAs on a GaAs substrate photomixer [26]. Adding a thin buffer layer of AlAs which has high thermal conductivity under the LTG-GaAs layer should be useful for improving the thermal property of the photomixer device [27].

2.3.4 Large Active Area

One method for improving the thermal damage threshold is to increase the active region of the photomixer. When the active region is large, the ohmic and optical heat density will be reduced. There is however, an important limitation for increasing the active area. The requirement of having a coherent CW THz source by photomixing is that the active area should be smaller than the operating frequency. When the active area is much larger than the wavelength of the generated THz, the perfect phase matching between the generated THz and the antenna will be difficult [13].

Using the array antenna in the photomixer device is one of the solutions to create a large active region. Each array element acts as a single small area photomixer, and the THz output waves from all the array elements combine together and form a synthesized wave of a phased-array antenna [13].

Another way to increase active area is to design a traveling-wave photomixer [28, 30, and 45]. In this structure, the generated THz waves in a large active area are coupled to the microwave transmission line which is connected to the active area which keeps the coherent superposition condition. Then, the generated THz waves can be radiated by an antenna connected to the end of the

transmission line. The traveling-wave photomixer can provide a very wide bandwidth because the transmission line's bandwidth is not limited by the electrode capacitance. Therefore, the traveling-wave photomixer can bypass the RC roll-off [28].

2.3.5 DC Electrical Characteristic

It is known that the THz output power is proportional with the square of the DC bias voltage. However, the effect of the bias voltage on the photomixer performance is dependent on many issues in the material properties and the non-uniform field distribution across the active region [22]. A higher DC bias voltage gives more THz power. However, the maximum bias field is limited by the break-down field threshold. The largest electric field which occurs at the surface of medium can be approximately calculated from the voltage bias divided by the gap width. The bias field distribution for a *Metal-Semiconductor-Metal* (MSM) planar electrode structure was studied in [29]. For a GaAs photomixer consisting of 0.2μm wide electrodes and 0.8μm wide gaps, the electric field distribution is shown in Figure 2.5.

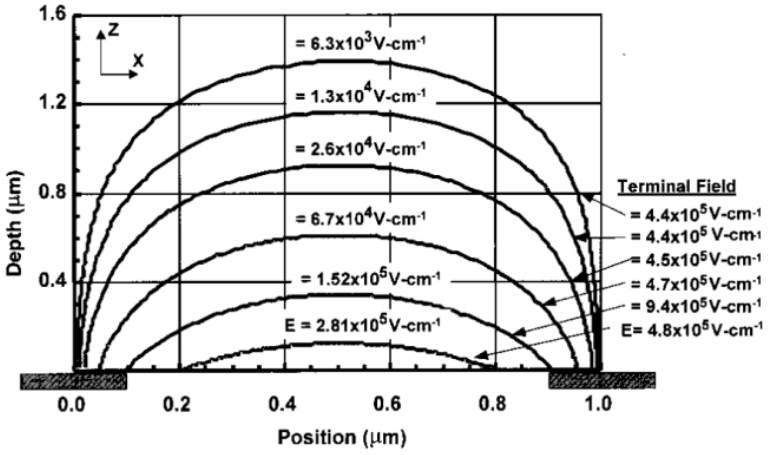

Figure 2.5 The electric lines of force between adjacent electrodes inside the 1.5 μm LTG-GaAs layer of an photomixer consisting of 0.2 μm wide electrodes and 0.8μm wide gap with a 40 V bias voltage.

As it can be seen in Figure 2.5, the electric field in the photomixer device is strong and is close to the electrodes and the top surface of the medium, but it decreases rapidly with the depth in the medium.

2.3.6 Laser Source and Coupling

The THz output power in photomixing is proportional to the total input power. This makes the laser type and wavelength, and the optical coupling to the active region of the photomixer device very critical and important concerns. Hence high power lasers with spectral purity and wide tunability are required for the photomixing process. The first lasers which have shown good results as optical sources in LTG-GaAs photomixers were the Ti:Sapphire lasers known as Ti:Al2O3 solid state lasers [20]. The Ti:Sapphire lasers have a 780nm center wavelength with at least 50nm of spectral tuning and can provide a high THz output power. The photomixers must have the capability of being compact and low power consumming THz sources. Thus the difficulty with the Ti:Sapphire laser is that the total system of this laser is large and has a large power consumption.

The diode lasers are a good choice to satisfy all the requirements such as being compact and low power consuming sources. The diode lasers though, need improvement in their spectral purity and frequency stability. However, the optical power of the frequency stabilized diode lasers is relatively low (around a few mW) for generating THz radiation [13].

The *Master Oscillator Power Amplifier* (MOPA) lasers have a high enough optical power level as optical sources for photomixers. However, compared to the Ti:Sapphire lasers, the MOPA has limited tunability [20].

As mentioned before, the optical coupling of the laser sources is a main issue in the photomixing efficiency. The goal is to focus the input power on the active region to avoid the reflection from metals or the air-photoconductor surface. As a result of the two dimensional grating of the electrodes, the first concern for optical coupling is the polarization. When the polarization of the incident fields are parallel to the lines of the electrodes grating, the incident fields of both lasers should be perpendicular to the electrodes [20].

2.3.7 THz Wave Coupling

The coupling of the generated THz radiation to the free space is one of the important issues in the integrated THz photomixer antenna devices. An effective and common way is to do this coupling is through a back side hemispheric lens made out of a high refractive index material [20]. A hyperhemispherical, high resistivity silicon lens attached to the backside of the substrate of the photomixer device can help to reduce the reflection from the air-photoconductor surface and increase the THz radiation efficiency. It should be mentioned that other free space coupling methods have

been considered but none of them have the hyperhemispherical lens' performance [20]. In the end, after the free space coupling, the free space THz wave can be shaped and guided with parabolic mirrors or waveguides.

Chapter 3
Photomixing Theory

The transport phenomena in photomixer devices can be modeled by a set of drift-diffusion equations. By solving these partial differential equations along with the appropriate boundary conditions, the distributions of the device's internal variables such as the carrier transport, current densities, potential, and electric field can be obtained. This chapter introduces the set of drift-diffusion equations and discusses the different processes required to solve such equations to obtain the generated THz photo-current in photomixer devices.

3.1 Introduction

In a photomixer device, two optical laser beams illuminate the photoconductive gap and generates time varying carrier densities. Under the effect of an applied bias voltage, the free carriers generate the THz photo-current there the photo-current is modulated according to the intensity of the optical beat. The photogenerated current is then fed into the integrated antenna. Finding the generated photo-current while considering all important physical phenomena related to the CW THz photomixer operation is an important issue in the photomixer device characterization. The analysis of the CW THz photomixer sources is a multi-facet problem that includes the semiconductor physics and the electromagnetic.

There are different models to analyze and simulate semiconductor devices. The drift-diffusion, Hydrodynamic, Thermodynamic and Monte Carlo model are some of them. One of the models can be selected depending on the device under investigation, and the level of complexity and accuracy required. The equations of most of the models are formulated initially under the Boltzmann statistics assumptions.

3.2 Semiconductor Equations

The basic semiconductor equations are a set of equations which are valid for many main applications in the device analysis [31]. In the photomixer device, the drift-diffusion model is used to find the generated THz photo-current; this model is defined by the basic semiconductor equations. The drift-diffusion model is commonly used for the simulation of the carrier transport in photo-conductive devices.

In this application, the drift-diffusion model can explain the physical phenomena inside the photoconductor such as the optical generation of the carriers and currents, and the filed-screening effect. Also this model is sufficiently simple in its numerical calculation and needs less computational time compared to other models [30].

The set of drift-diffusion equations include Poisson's equation, the continuity equations for electrons and holes, and the current relations for electrons and holes as follows [31]:

$$\nabla.\varepsilon\nabla\Phi = q(n - p - C_t) \tag{3.1}$$

$$q\frac{\partial n}{\partial t} = \nabla.\vec{J}_n + q(-R + G) \tag{3.2a}$$

$$q\frac{\partial p}{\partial t} = -\nabla.\vec{J}_n + q(-R + G) \tag{3.2b}$$

$$\vec{J}_n = -q\mu_n n\nabla\Phi + qD_n\nabla n \tag{3.3a}$$

$$\vec{J}_p = -q\mu_p p\nabla\Phi - qD_p\nabla p \tag{3.2b}$$

where $\boldsymbol{\Phi}$ is the electrostatic potential, n and p are the electron and hole carrier concentrations, q is unit charge, ε is electrical permittivity, C_t is net trap concentration filled by the charge inside the semiconductor, R is the carrier recombination rate, G the is carrier generation rate, J_n and J_p are the electron and hole current densities, D_n and D_p are the electron and hole diffusion coefficients and μ_n and μ_P are the electron and hole motilities.

Substituting the current equations into the continuity equations from the set of the drift-diffusion equations, one can obtain three partial differential equations with dependent variables of n, p, and $\boldsymbol{\Phi}$. The equations are as follows [30]:

$$\nabla.\varepsilon\nabla\Phi = q(n - p - C_t) \tag{3.4}$$

$$\frac{\partial n}{\partial t} = \nabla.(D_n\nabla n - n\mu_n\nabla\Phi) - R + G \tag{3.5a}$$

$$\frac{\partial p}{\partial t} = \nabla.\left(D_p\nabla p + p\mu_p\nabla\Phi\right) - R + G \tag{3.5b}$$

The above equations are solved for the electrostatic potential ($\boldsymbol{\Phi}$) and the carrier concentrations (n and p).

Note that, when the cross sectional dimension of the device is comparable with the operating wavelength, the Poisson's equation may not give an accurate representation of the electric field in

terms of the distributed time varying charges. In that case, the wave equations should be used instead of Poisson's equations. Therefore, the new set of equations is as follows: [30]

$$\nabla \times \nabla \times E + \mu\varepsilon \frac{\partial^2 E}{\partial^2 t} = -\mu \frac{\partial}{\partial t} \left(J_n + J_p\right) \tag{3.6}$$

$$q \frac{\partial n}{\partial t} = \nabla . \vec{J}_n + q(-R + G) \tag{3.7a}$$

$$q \frac{\partial p}{\partial t} = -\nabla . \vec{J}_n + q(-R + G) \tag{3.7b}$$

$$\vec{J}_n = -q\mu_n n \nabla \Phi + qD_n \nabla n \tag{3.8a}$$

$$\vec{J}_p = -q\mu_p p \nabla \Phi - qD_p \nabla p \tag{3.8b}$$

3.2.1 Generation-Recombination Process

Carrier Generation/Recombination is an important process in semiconductor devices. There are different models for the Generation/Recombination phenomena. But the *Shockley Read Hall* (SRH) and Auger models have important roles in analyzing the semiconductor device behavior.

The SRH process is caused by the absorption or emission of phonons. This process is trap assisted utilizing a lattice defect at the trap energy level within the semiconductor band gap. In this model, four sub-processes are possible [31]:

- Electron capture: An electron from the conduction band is captured by an empty trap in the band-gap of the semiconductor.
- Hole capture: The trapped electron moves to the valence band and neutralizes a hole.
- Hole emission: An electron from the valence band is trapped leaving a hole in the valence band.
- Electron emission: A trapped electron moves from the trap energy level to the conduction band.

As it can be seen, the Generation/Recombination process is done with the help of traps.

The total Generation/Recombination is given by [31]:

$$R_{net}^{SRH} = R_n - G_n = R_p - G_p \tag{3.9}$$

Since the electrons and holes are in pairs, their net Generation/Recombination rate must be equal.

Therefore, the net Generation/Recombination rate, R_{net}, can be found by [31]:

$$R_{net}^{SRH} = \frac{np - n_{i,eff}^2}{\tau_p(n+n_1)+\tau_n(p+p_1)} \tag{3.10}$$

$$n_1 = n_{i,eff}\, exp\left(\frac{E_{trap}}{kT}\right) \tag{3.11}$$

$$p_1 = n_{i,eff} \exp\left(\frac{-E_{trap}}{kT}\right) \tag{3.12}$$

where E_{trap} is the difference between the defect energy level and the intrinsic energy level, τ_n and τ_p are the electron and hole carrier lifetimes, and n_i is the intrinsic carrier concentration.

The Auger Generation/Recombination is the other model which is important in device modeling. The Auger Generation/Recombination is typically important at high carrier densities. The direct band-to-band Auger process involves three particles. During generation, an electron hole pair is generated consuming the energy of a highly energetic particle. In recombination, when an electron hole pair recombines, the resulting energy is transferred to another electron or hole. The four partial processes can be explained as follows [31]:

- Electron capture: An electron from the conduction band moves to the valence band and recombines with a hole in the valence band. The excess energy is transferred to another electron in the conduction band.
- Hole capture: An electron from the conduction band moves to the valence band and recombines with a hole. The excess energy is transferred to another hole in the valence band.
- Electron emission: A highly energetic electron from the conduction band releases its energy to an electron in the valence band. The valence electron moves to the conduction band and leaves a hole in valence band.
- Hole emission: A highly energetic hole from the valence band releases its energy to an electron in the valence band. The valence electron moves to the conduction band and leaves a hole in valence band edge.

The total Auger Generation/Recombination rate is the sum of the net rates for the electrons and holes [31]:

$$R_{net}^{Au} = R_n - G_n + R_p - G_p \tag{3.13}$$

Therefore, the Auger Generation/Recombination rate can be obtained by:

$$R_{net}^{Au} = \left(nC_n + pC_p\right)\left(np - n_i^2\right) \tag{3.14}$$

where C_n and C_p are Auger capture coefficients for the electron and hole respectively.

3.2.2 Optical Generation Rate

When a photoconductor is illuminated by an optical propagation, the photon absorption generates electron and hole pairs. The photocarrier generation rate is given by [22]:

$$G(r,t) = \alpha \frac{I(r,t)}{h\nu} = \alpha \frac{E^2(t)}{\eta_0 h\nu} \tag{3.15}$$

where α is the absorption coefficient, $h\nu$ is the optical photon energy, η_0 is the intrinsic impedance of the medium, $E(t)$ is the optical electric field measured in the medium at point r where the absorption occurs and $I(r,t)$ is the optical power density.

By linear superposition, the $E(t)$ consists of the two independent optical fields E_1 and E_2. E_1 and E_2 are the field amplitudes of two independent optical excitations. If φ is the phase difference between the two fields, ω_1 and ω_2 are the angular frequencies of two optical excitations respectively, and $\Delta\omega$ is the angular frequencies difference, the photocarrier generation rate can be written:

$$G(r,t) = \alpha \frac{[E_1(t)+E_2(t)]^2}{\eta_0 h\nu} = \frac{\alpha}{\eta_0 h\nu}\{\frac{E_1^2(1+cos2\omega_1 t)}{2} + \frac{E_2^2(1+cos\,(2\omega_2 t+\varphi))}{2}$$
$$+E_1E_2\,cos(\Delta\omega t-\varphi) + E_1E_2\,cos\left((\omega_1+\omega_2)t+\varphi\right)\} \tag{3.16}$$

The fast oscillating terms are ignored because of the slow response of the photoconductivity. Therefore, for the photomixing, it suffices to consider the averaged optical intensity and the optical beat intensity with the difference frequency, $\Delta\omega$.

$$G(r,t) = \alpha \frac{[E_1(t)+E_2(t)]^2}{\eta_0 h\nu} = \frac{\alpha}{\eta_0 h\nu}\left[\frac{E_1^2}{2} + \frac{E_2^2}{2} + E_1E_2\,cos(\Delta\omega t-\varphi)\right] =$$
$$\frac{\alpha}{h\nu}\left[I_1 + I_2 + 2\sqrt{I_1 I_2}\,cos(\Delta\omega t-\varphi)\right] \tag{3.17}$$

where I_1 and I_2 are the time-averaged intensities of each field at the absorption point. It can be proved that the photocarrier generation rate is at maximum when $I_1 = I_2$. Then the generation rate will be:

$$G(r,t) = \frac{2\alpha I_1}{h\nu}\left[1 + cos(\Delta\omega t-\varphi)\right] \tag{3.18}$$

3.2.3 Boundary Conditions

For solving the basic semiconductor equations, the appropriate boundary conditions must be considered to obtain the electric potential and carrier concentrations.

In Photomixer device simulations, Semiconductor-Metal Boundaries, Insulator-Metal Boundaries, and Semiconductor-Insulator Boundaries should be considered.

3.2.3.1 Semiconductor-Metal Boundaries

Ohmic Contacts:

The Dirichlet boundary condition is applied at ohmic contact and fixes the basic variables $\boldsymbol{\Phi}$, n, and p at the given values. The boundary conditions for these basic variables are given by [30]:

$$\Phi = \Phi_b + \Phi_a \tag{3.19}$$

$$n = \frac{1}{2}\left[\sqrt{(N_D^+ - N_A^-)^2 + 4n_i^2} + (N_D^+ - N_A^-)\right] \tag{3.20}$$

$$p = \frac{1}{2}\left[\sqrt{(N_D^+ - N_A^-)^2 + 4n_i^2} - (N_D^+ - N_A^-)\right] \tag{3.21}$$

where $\boldsymbol{\Phi}_b$ is the built-in potential due to the fixed charge distribution $(N_D^+ - N_A^-)$ and $\boldsymbol{\Phi}_a$ is the bias potential applied to the metal contacts.

In the interface of the metal and semiconductor, the boundary condition for the ohmic contacts is characterized by the vanishing total space charge in the semiconductor at the interface. Hence, there is no impressed charge accumulation at the interface, and the incoming carriers to the boundary can move freely in both directions, depending on the applied potential [30].

Schottky Contacts:

The mixed boundary conditions are applied at the Schottky contacts. A typical model for the Schottky contacts is presented here. The Schottky contact boundary conditions are given by [37]:

$$\Phi = \Phi_a - \Phi_w \tag{3.22}$$

$$\vec{J}_n.\hat{n} = qv_n(n - n_s) \qquad \vec{J}_p.\hat{n} = -qv_p(p - p_s) \tag{3.23}$$

$$n_s = N_C\, exp\left(\frac{-E_C - E_w}{kT}\right) \qquad p_s = N_V\, exp\left(\frac{E_V - E_w}{kT}\right) \tag{3.24}$$

where $\boldsymbol{\Phi}_w$ is the metal work function difference potential, which can be derived from the work function difference energy E_w:

$$\Phi_w = -\frac{E_w}{q} \tag{3.25}$$

Here v_n and v_p are the thermionic recombination velocities, n_s and p_s are the carrier contact concentrations, E_C and E_V are the conduction and valence band energies, and $\hat{n}$ is the unit normal vector at the boundary.

3.2.3.2 Insulator-Metal Boundaries

At the insulator-metal boundaries a model similar to the Schottky contact model is used to calculate the insulator contact potential.

$$\Phi = \Phi_a - \Phi_w \tag{3.26}$$

3.2.3.3 Semiconductor-Insulator Boundaries

At the interface between a semiconductor and an insulator, the boundary conditions are given by [30]:

$$\varepsilon_{semi} \frac{\partial \Phi}{\partial n}|_{semi} - \varepsilon_{ins} \frac{\partial \Phi}{\partial n}|_{ins} = \rho_s \tag{3.27}$$

$$\vec{J}_n . \hat{n} = -eR^{Surf} \tag{3.28}$$

$$\vec{J}_p . \hat{n} = eR^{Surf} \tag{3.29}$$

where ε_{semi} and ε_{ins} are the semiconductor and the insulating material permittivities respectively ρ_s is the surface charge density at the interface and R_{Surf} is the surface recombination rate.

Chapter 4
CW THz Photomixer Source Simulation

Photomixer source modeling is a multifaceted problem involved with both semiconductor and electromagnetic parts. Most of the researches on modeling of photomixer structures focus on one part and make simplistic assumptions for the other aspect of the problem. Hence, it is crucial to analyze and model the photomixer source while rigorously considering both aspects of the device modeling. Other than a few researches devoted to rigorously incorporate all physical aspects of the photomixer devices in the modeling [38, 39], most of the researches report either the experimental results or simple analytical models to investigate the device performances. In this chapter, a computational simulation method is presented to model and analyze integrated THz photomixer antenna. The presented computational simulation method combines a semiconductor solver, such as TCAD Sentaurus, and a full-wave electromagnetic simulator, such as HFSS, to rigorously analyze an integrated THz photomixer antenna. Developing such a computational methodology mainly contributes in photomixer source modeling and performance analysis in a rigorous manner, and also provides an optimization procedure as a pre-fabrication process.

To obtain the generated THz photo-current inside the photomixer device, a set of drift-diffusion equations presented in Chapter 3 should be solved. For solving the basic drift-diffusion equations, a semiconductor device simulator, is used. In this chapter, the aim is to employ a semiconductor solver to obtain THz photo-current inside the photoconductive layer of photomixer structure. The generated photo-current is modeled as a current source in the antenna design to calculate the radiated THz power from photomixer device. The THz antenna geometry and input impedance calculations are performed in an electromagnetic solver. To investigate the effects of photomixer structure parameters on the THz photo-current and radiated power, the photomixer parameters such as carrier lifetime of material, applied optical power density, applied bias voltage, the operating frequency, and the gap size are analyzed.

4.1 Introduction

In this chapter, my attempt is to analyze and characterize the CW THz photomixer source using the presented computational simulation method. A schematic of a typical CW THz photomixer structure is shown in Figure 4.1. As mentioned in section 2.3.2, different types of antenna can be employed for

THz radiations [15, 20, 21, 26 and 46]. In Figure 4.1, without the loss of generality, a bow-tie antenna is excited by either a simple photoconductive gap or interdigitated-electrodes.

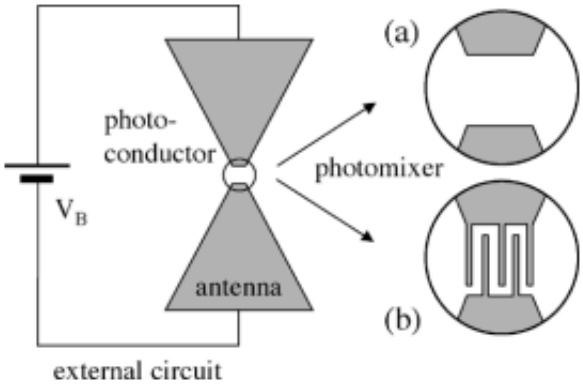

Figure 4.1 The schematic diagram of a CW THz photomixer, consisting of an antenna coupled to the external circuit, with two designs for electrodes: (a) simple photoconductive gap and (b) interdigitated-electrodes [21].

Since the optical waves are involved in photomixing process, the optical resolutions should be considered in semiconductor solver, whereas the radiating antenna should be modeled at THz scale which is a few hundred times larger than the optical scale. Thus, modeling the whole antenna structure in the semiconductor solver is computationally costly and time-consuming. Since the optical to THz conversion efficiency is very low, the antenna structure would not significantly affect the photomixing process. Therefore, for the sake of simulation efficiency, the feed point of the antenna can be focused and considered as the simulation geometry in the semiconductor solver. Then, the generated THz photo-current at the feed point can be applied to the radiating antenna at the THz frequency in the electromagnetic solver. In this thesis, without the loss of the generality, three different photomixer devices are modeled; 1) the CW THz photomixer with a simple photoconductive gap, 2) the CW THz photomixer with interdigitated-electrodes, and 3) the array antenna configuration of the THz photomixer. These different structures are modeled and analyzed, and the results are discussed.

4.2 Photomixer Model and Analysis

TCAD Sentaurus is a comprehensive device simulator which is capable of simulating the electrical, optical, and thermal characteristics of semiconductor devices. TCAD Sentaurus also includes the *Electromagnetic Wave Solver* (EMW) module which solves Maxwell's equations using the *Finite*

Difference Time Domain (FDTD) method (see Appendix A). The EMW module can be employed to obtain electromagnetic fields in the photomixer and consequently to calculate the time-averaged optical generation rate, G_{av}, through the following equation:

$$S_{av} = \frac{1}{2} Re(ExH^*) \tag{4.1}$$

$$W = -\nabla . S_{av} = \frac{1}{2}\sigma |E|^2 \tag{4.2}$$

$$G_{av} = \eta \frac{W}{h\nu} \tag{4.3}$$

where S_{av} is the time-averaged poynting vector, W is the power flux density, and σ is the conductivity.

Note that the EMW module is able to calculate the time-averaged optical generation rate G_{av}, whereas the time-dependent optical generation rate should be included in equation (3.5). The optical generation rate as a function of THz frequency is presented in equation (3.18). Having G_{av} calculated by the EMW module, the time-varying optical generation, G can be generated. Applying the THz frequency to G_{av}, the Sentaurus Device simulator is able to include the time-varying G in the set of drift-diffusion equations which are to be numerically solved in the time domain. By solving the electron and hole current continuity equations coupled to the Poisson's equation, the electrostatic potential and photocarrier generation rate can be obtained in the photomixer device. The calculated quantities can then be used to characterize and analyze various parameters of the photomixer such as the radiated THz power.

By solving the set of drift-diffusion equations, the total current density is obtained by:

$$\vec{J} = \vec{J}_n + \vec{J}_p + \vec{J}_D \tag{4.4}$$

where $\vec{J}_D$, $\vec{J}_n$, and $\vec{J}_p$ is the displacement current, electron current, and hole current density, respectively. The 2D total current in Sentaurus Device is calculated according to the approach proposed by Palm and Van de Wiele [41].

4.2.1 Photomixer with Simple Photoconductive Gap

In this section, a photomixer with a single photoconductive gap is simulated (see Appendix B). The cross section of the photomixer structure is shown in Figure 4.2. It consists of two metallic strips with the width of *w* and thickness of *h* running in parallel on a dielectric substrate with the thickness of *t*. The strips are separated with the gap, *g*. The metallic strips also act as biasing electrodes, and a DC

bias voltage, V_{DC}, is applied to the electrodes to provide the required DC electric field for photo-current excitation. The metal strips are made of gold (Au). Gold is used in the photomixer structure because of its higher electrical and thermal conductivity [20]. The substrate material used in the photomixer device is LTG-GaAs.

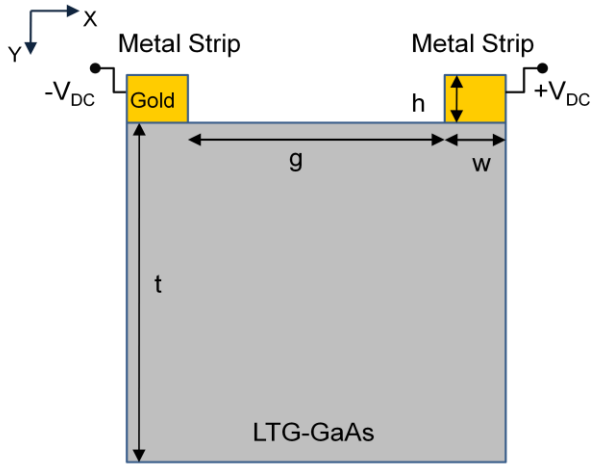

Figure 4.2 The cross section view of a modeled MSM photomixer.

The device is illuminated by two optical plane wave excitations whose frequency difference falls in the THz region. The *Absorbing Boundary Conditions* (ABCs) are applied to all four sides of the simulation domain. Since the boundary condition is absorbing, the size of strip widths does not affect the simulation results. It has been confirmed by simulating the same structure with different strip widths. Therefore, the strip width is chosen to be small to save simulation run time. For the designed structure, the total applied optical power density is 0.4 mW/μm^2 and the applied bias voltage is 20V. Also the beat frequency is 0.5 THz.

The physical parameter of the modeled photomixer with LTG-GaAs substrate is given in Table 4.1.

Table 4.1 The physical parameters of the modeled LTG-GaAs photomixer

Parameter	Value
Operating temperture, T_0	300 K
Laser central wavelength, λ	800 nm
Optical Power density, I_0	0.4 mW/μm^2
Absorption coefficient	10000 cm^{-1} *
Low field electron lifetime, τ_{n0}	1ps *
Low field hole lifetime, τ_{p0}	1ps *
Electron saturation velocity, v_{n0}	4x10^4 m/s *
Hole saturation velocity, v_{p0}	4x10^4 m/s *
Low field electron mobility, μ_{n0}	20000 cm^2/Vs *
Low field hole mobility, μ_{p0}	50 cm^2/Vs *
Relative permittivity, ε_r	13.18 *
Gap size, g	1 μm
Strip thickness, h	0.2 μm
Strip width, w	0.2 μm
Substrate thickness, t	1.5 μm

Refrence: * TCAD Sentaurus material library

Using the EMW solver, the time-averaged carrier generation rate inside the LTG-GaAs layer is shown in Figure 4.3. The carrier generation rate is not uniform and the effect of scattering from the edges can be seen in the result.

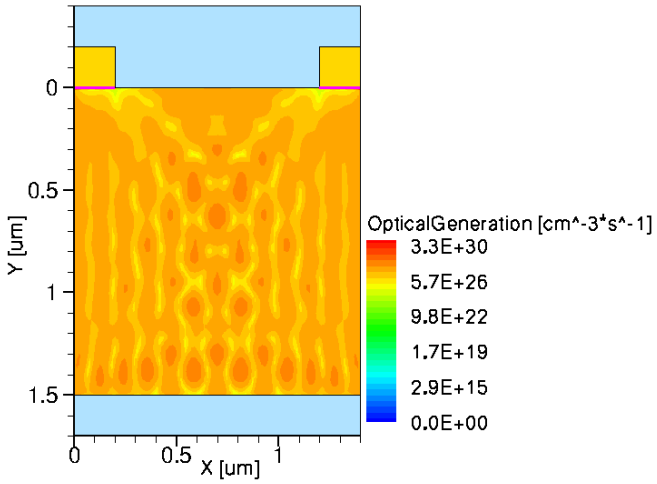

Figure 4.3 The time-avereged carrier photogeneration inside the LTG-GaAs layer of photomixer at 0.5 THz The total optical power density is 0.4 mW/μm^2.

Using semiconductor device simulator, the THz photo-current can be obtained in the photomixer device. The total generated THz photo-current has two components, the DC component, and the THz component ($I_{THz} = I_{DC}+I_{AC}$). The maximum DC photo-current is limited by the maximum DC bias and optical power before device failure occurs [39]. The transverse DC photo-current versus the applied bias voltage is shown in Figure 4.4. The total applied optical power density is 0.4mW/μm^2, and the beat frequency is 0.5 THz. As can be seen in Figure 4.4, the DC photo-current in the LTG-GaAs photomixer has approximately a linear dependency on the bias voltage at lower bias voltages. Note that, the applied DC bias voltage is limited to the LTG-GaAs breakdown field which is around 500 kV/cm [20, 25].

By solving the electron and hole current continuity equations coupled with the Poisson's equation, different parameter values of the photomixer device can be found. The total transverse THz photo-current versus the time is illustrated in Figure 4.5. As presented in (4.4), the total THz current density is the summation of the electron current density ($\vec{J}_n$), hole current density ($\vec{J}_p$), and displacement current density ($\vec{J}_D$).

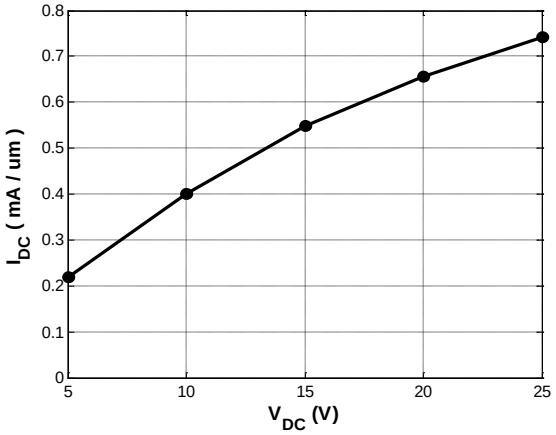

Figure 4.4 The transverse DC photo-current in LTG-GaAs photomixer for different bias voltage. The total applied optical power density is 0.4 mW/μm^2.

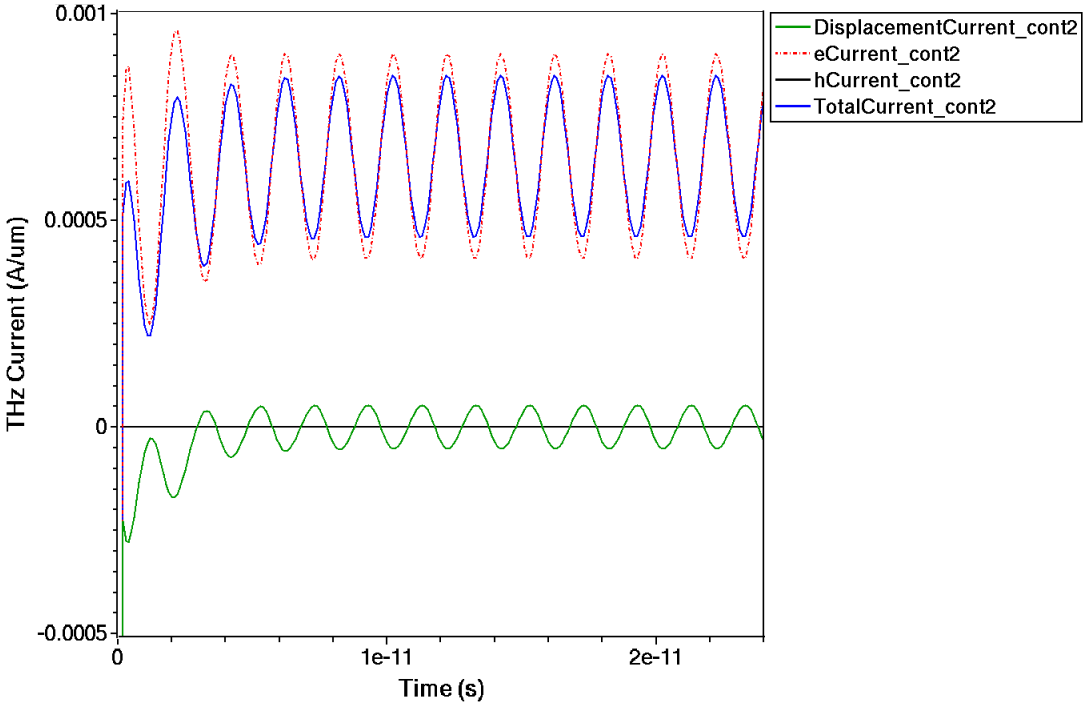

Figure 4.5 The THz photo-current at electrodes versus the time for 20V bias voltage at 0.5 THz. The total optical power density is 0.4 mW/μm^2.

Figure 4.6 shows the current density distribution inside the LTG-GaAs layer of the photomixer. The applied bias voltage is 20V and the total applied optical power density is 0.4mW/μm^2. Also the beat frequency is 0.5 THz. Note that, Figure 4.6 shows a snapshot of the current distributions inside the LTG-GaAs layer.

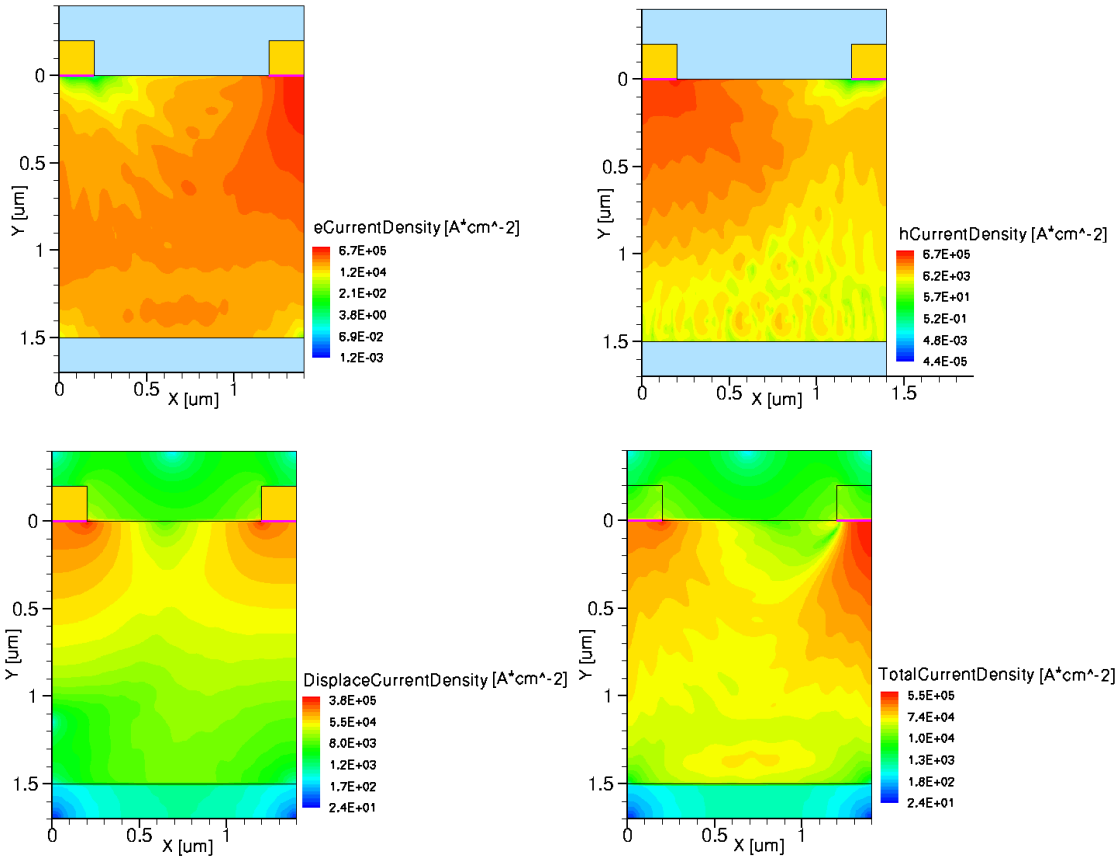

Figure 4.6 The Electron Current Density, Hole Current Density, Displacement Current Density, and Total Current Density respectively inside the LTG-GaAs layer of photomixer.

A snapshot of the electric field distribution inside the structure is also shown in Figure 4.7.

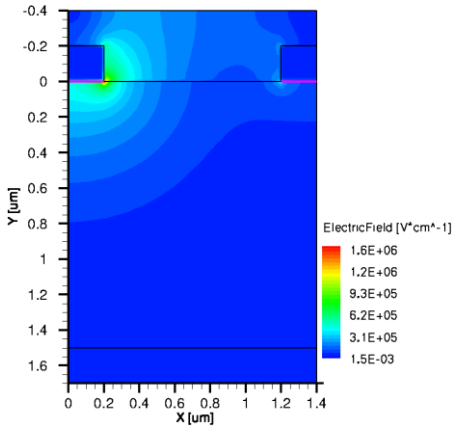

Figure 4.7 The Electric Field distribution for a 20V bias voltage at 0.5 THz.

The total optical power density is 0.4mW/μm^2.

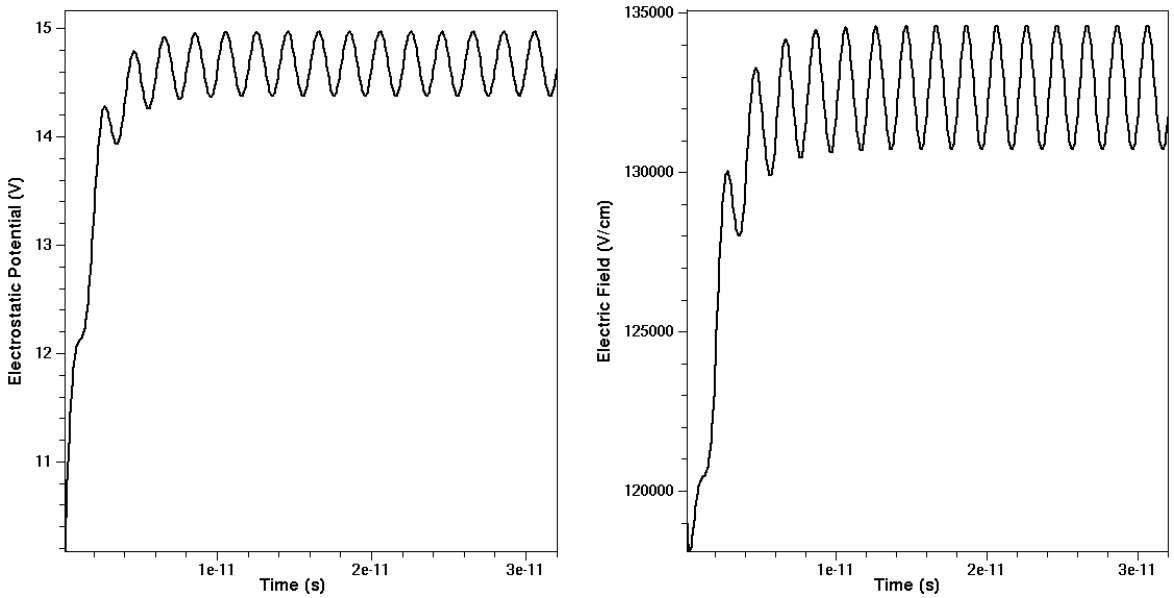

Figure 4.8 The Electrostatic Potential and Electric Field versus the time at 20V bias voltage at 0.5 THz. The total optical power density is 0.4 $mW/\mu m^2$.

The electrostatic potential is computed from solving the continuity equations coupled to the Poisson's equation. The obtained electrostatic potential and electric field are shown in Figure 4.8 for a certain point located in the gap on the LTG-GaAs surface.

The THz photo-current amplitude versus the bias voltage for different THz beat frequencies is plotted in Figure 4.9. As can be seen in the graphs, the THz photo-current is increased when applying higher bias voltage. Additionally, THz photo-current would be larger for lower beat frequencies. Also, larger THz photo-current is generated at lower frequencies. This behavior has been shown experimentally by E. Brown et al. [43]. However, the maximum applied field is restricted by the threshold field break-down in the LTG-GaAs material which is around 500 kV/cm.

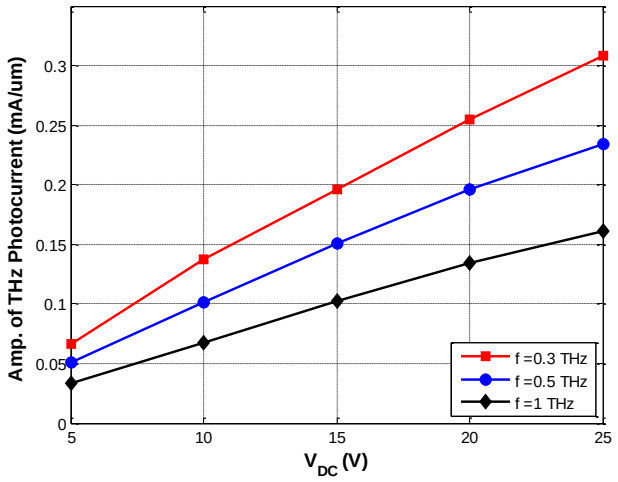

Figure 4.9 The amplitude of the THz photo-current versus the bias voltage for different THz frequencies. The total optical power density is 0.4mW/μm^2.

The amplitude of the THz photo-current is illustrated in Figure 4.10 as a function of the carrier lifetime in the LTG-GaAs photomixer. These plots are in well-agreement with [21]. As can be observed, the optimum carrier lifetime, for which the maximum THz photo-current is obtained, reduces at a higher frequency. This optimum value is of the order of THz signal period. If the carrier lifetime is very short, the fast carrier recombination does not provide a significant modulation in the conductivity. However, if the carrier lifetime is larger than the THz period, the charge accumulation increases the device heating [21].

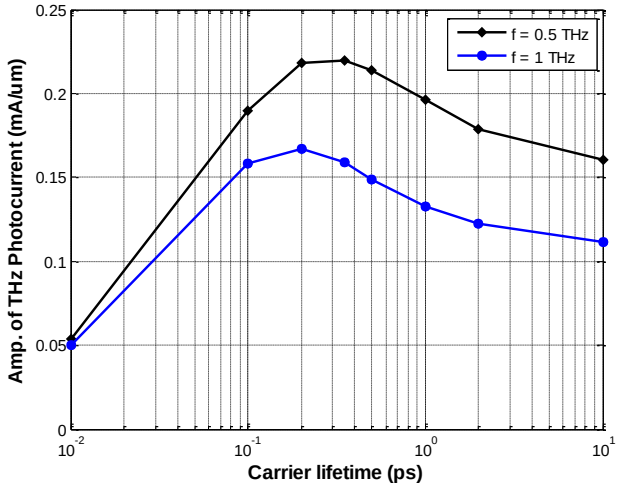

Figure 4.10 The amplitude of the THz photo-current versus the carrier lifetime for 20V bias voltage at 0.5 THz. The total optical power density is 0.4mW/μm^2.

Figure 4.11 shows the amplitude of the THz photo-current versus the bias voltage for different photoconductive gap sizes. If the gaps are made smaller to shorten the transit time required to increase the photoconductive gain, the device capacitance increases and limits the THz power through the RC roll-off. Additionally, small gaps cause thermal failure in the device. If the gaps are made larger to decrease the device capacitance, the transit time increases and then the associated photoconductive gain reduces, limits the THz output power. In fact, selecting the optimum gap size is a trade-off between the photoconductive gain, the RC roll-off, and the heat dissipation.

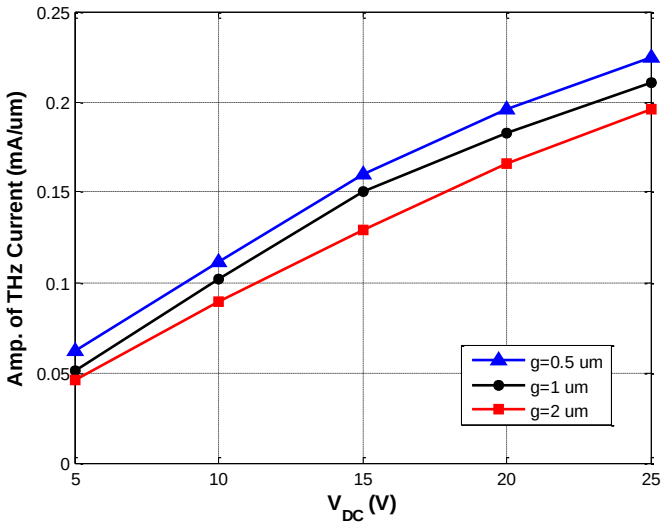

Figure 4.11 The amplitude of the THz photo-current for different photoconductive gap sizes at 0.5 THz. The total optical power density is 0.4mW/μm^2.

The amplitude of the THz photo-current versus the beat frequency is illustrated in Figure 4.12. As expected, the THz photo-current decreases at high frequencies.

The amplitude of the THz photo-current versus the total optical power density is illustrated in Figure 4.13. The THz current increases with the optical power density. However, the thermal damage threshold of the LTG-GaAs material is limited to the optical power density of 1 mW/μm^2 [26].

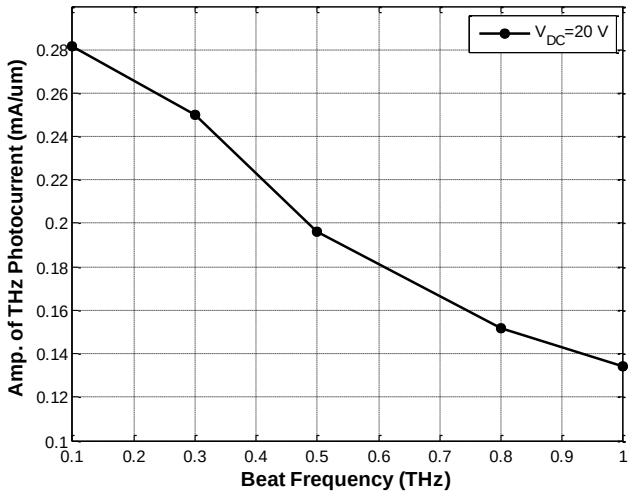

Figure 4.12 The amplitude of the THz photo-current versus the beat frequency. The total optical power density is 0.4mW/μm^2.

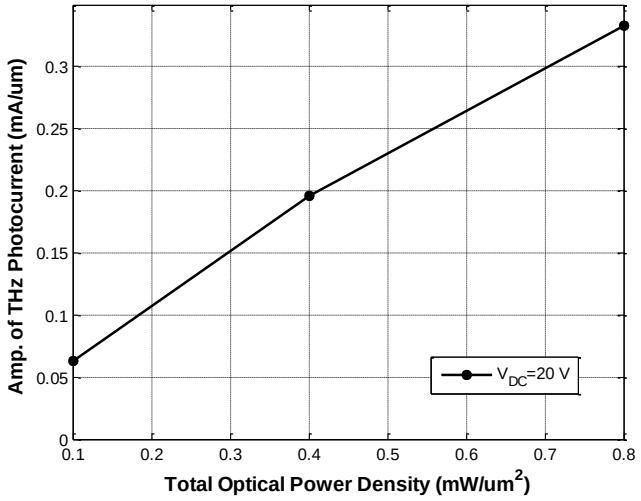

Figure 4.13 The amplitude of the THz photo-current versus the total optical power density at 0.5 THz.

4.2.2 Interdigitated-Electrode Photomixer

The active area of photomixer can be increased by adding interdigitated fingers to the electrodes. In photomixers with interdigitated-electrodes, the gap between the neighboring electrodes is comparable to or larger than the electrode width. Therefore, the most of the incident light enters the photoconductive material. The interdigitated finger electrodes in the photomixer design distribute the electric field uniformly in the semiconductor devices.

In this section, the interdigitated-electrode photomixer device simulation is discussed. Figure 4.14 shows the cross section of an interdigitated-electrode photomixer. The photomixer consists of three metal interdigitated-electrodes made of Gold deposited on the LTG-GaAs layer. The gap spacing between neighboring electrodes is 0.8 μm, and the electrode width is 0.2 μm for the given structure.

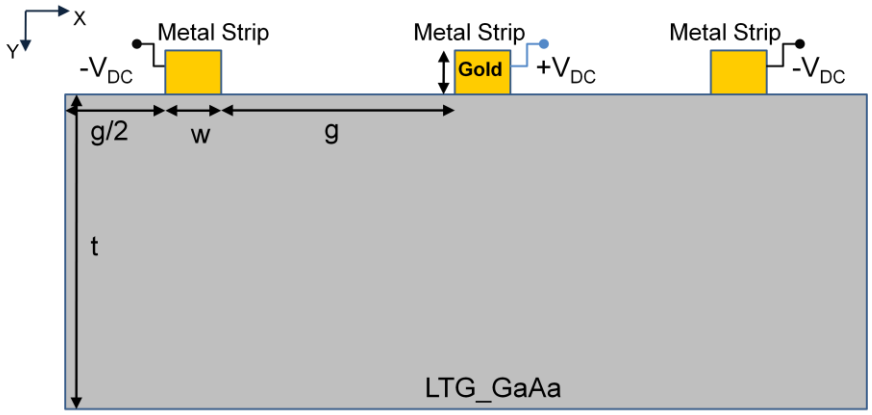

Figure 4.14 The cross sectional view of an interdigitated-electrode photomixer.

The physical parameter of the interdigitated-electrode photomixer with the LTG-GaAs substrate is given in Table 4.2. The parameters of LTG-GaAs material are the same as values in Table 4.1.

The photomixer device is illuminated by two optical plane wave excitations. The absorbing boundary conditions are applied to the simulation domain. For the designed structure, the total applied optical power density is 0.4 mW/μm^2, the applied bias voltage between the electrodes is 20V, and the beat frequency is 0.5 THz.

Figure 4.15 shows the transverse DC photo-current versus the applied bias voltage between the electrodes in the interdigitated-electrode photomixer.

Table 4.2 Pysical parameters of the modeled interdigitated-electrode photomixer made of LTG-GaAs

Parameter	Value
Operating temperture, T_0	300 K
Laser central wavelength, λ	800 nm
Optical Power density, I_0	0.4 mW/μm^2
Number of electrodes	3
Gap size, w_g	0.8 μm
Strip thickness, h_e	0.2 μm
Strip width, w_e	0.2 μm
Substrate thickness, d_t	1.5 μm

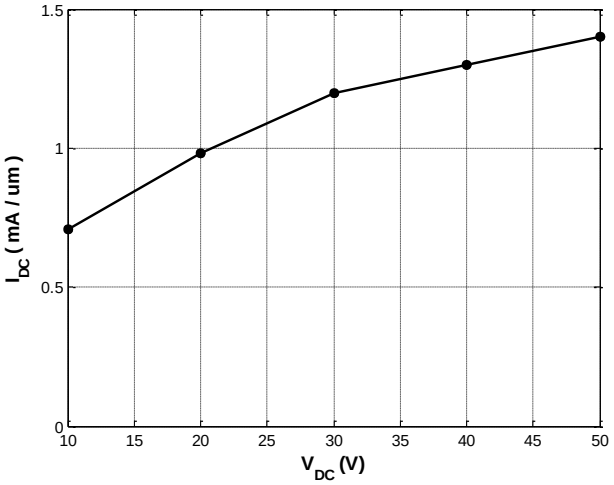

Figure 4.15 The transverse DC photo-current of the interdigitated-electrode photomixer. The total applied optical power density is 0.4 mW/μm^2.

The total transverse photo-current versus the time is illustrated in Figure 4.16. It shows the total photo-current on the central electrode of the photomixer device.

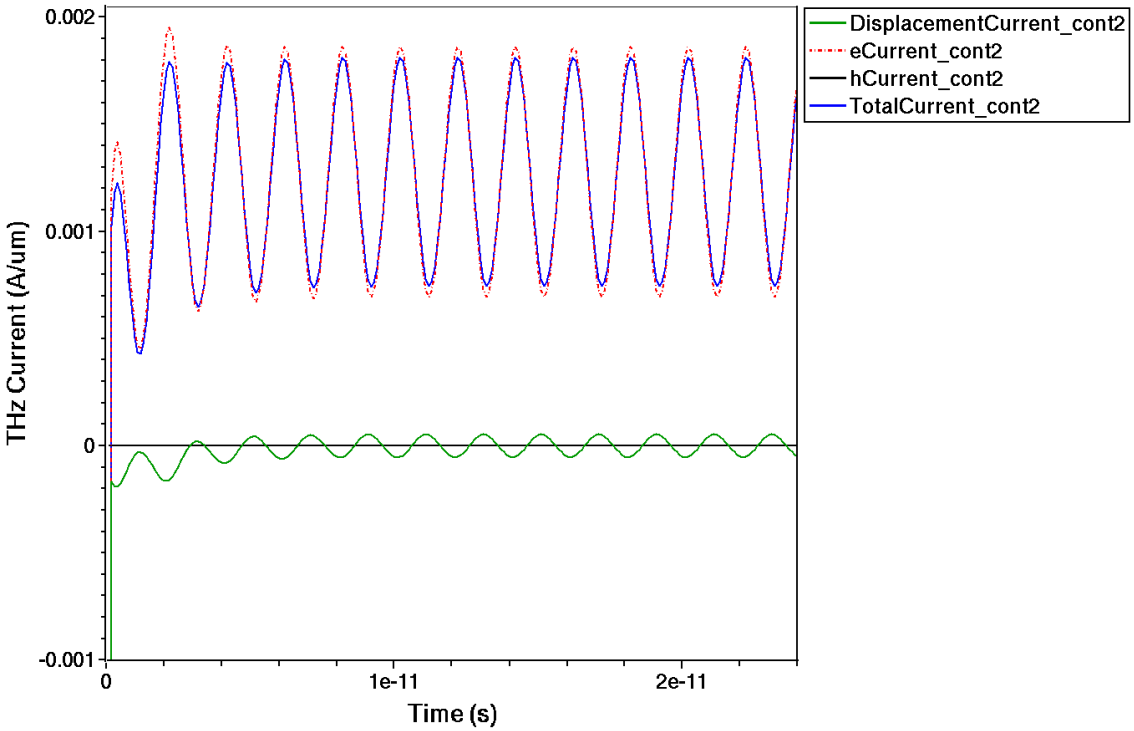

Figure 4.16 The total generated THz photo-current at the electrodes versus the time at 0.5 THz. The total optical power density is 0.4 mW/μm^2.

Figure 4.17 shows a snapshot of the distribution of electron and hole current densities inside the LTG-GaAs layer. The electron current density is concentrated on the central electrode with positive DC bias voltage and the hole current density is concenterated on the side electrodes with negarive DC bias voltages.

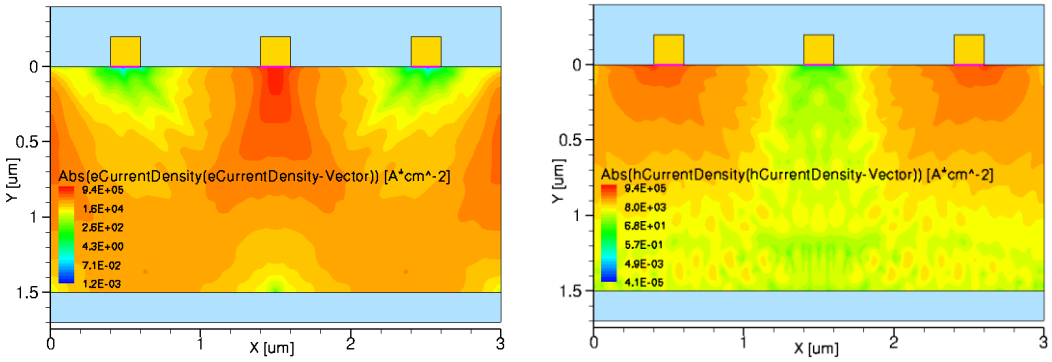

Figure 4.17 The Electron Current Density and Hole Current Density in the LTG-GaAs layer. The total optical power density is 0.4mW/μm^2, and the beat frequency is 0.5 THz.

The amplitude of the transverse THz photo-current versus the bias voltage between the electrodes is illustrated in Figure 4.18. As expected, the interdigitated-electrode photomixer device generates a higher THz photo-current compared to the single gap photomixer device.

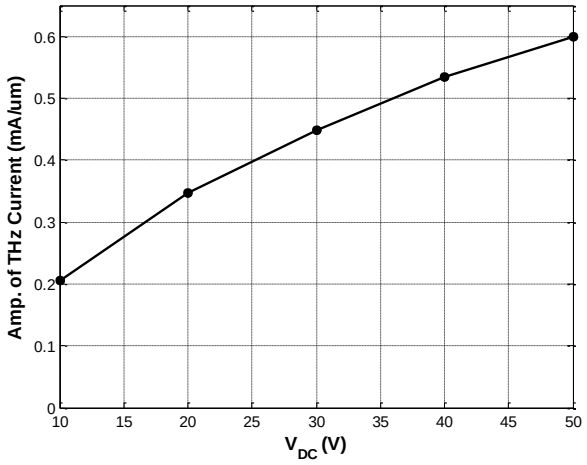

Figure 4.18 The amplitude of the transverse THz photo-current of the interdigitated-electrode photomixer versus the bias voltage at 0.5 THz. The total optical power density is 0.4 mW/μm^2.

The amplitude of the transverse THz photo-current versus the beat frequency is shown in Figure 4.19. The bias voltage between the electrodes is 20V. As it can be seen, the THz photo-current decreases at high frequencies.

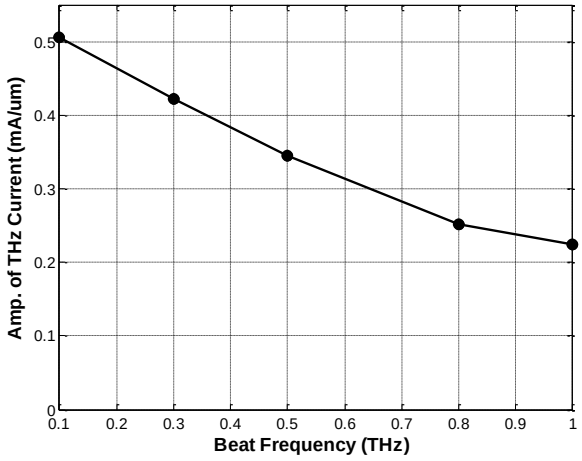

Figure 4.19 The amplitude of the THz photo-current versus the beat frequency.
The total optical power density is 0.4mW/μm^2.

4.2.2.1 Simulation Verification

An approximate theoretical model for interdigitated-electrode photomixer has been provided by E. Brown et al [14]. For verification purposes, the result of proposed computational simulation method can be compared with the result obtained by the approximate theoretical model. According to this theoretical model, the time-dependent photomixer conductance (G_p) can be approximated by [14]:

$$G_p \approx \frac{\eta T \tau N_g^2 (\mu_e + \mu_h) P_0}{h\nu (N_e w_e + N_g w_g)^2} \left(1 + \frac{2\sqrt{mP_1P_2}\sin(\Delta\omega t + \varphi)}{P_0\sqrt{1+\Delta\omega^2\tau^2}}\right) \tag{4.5}$$

where N_g is the number of gaps, N_e is the number of electrodes, w_g is the gap width, w_e is electrode width, T is the optical power transmissivity, and P_0 is the total optical power.

By substituting the physical parameters of the photomixer structure, the G_p can be calculated through the equation (4.5). For comparison purposes, the time-dependent conductance, defined as dividing the generated THz photo-current by the bias voltage, is obtained for the simulated results of the proposed method. The two time-dependent conductances are plotted in Figure 4.20. Although the results are approximately of the same order, the approximate theory obviously overestimates the time-dependent conductance.

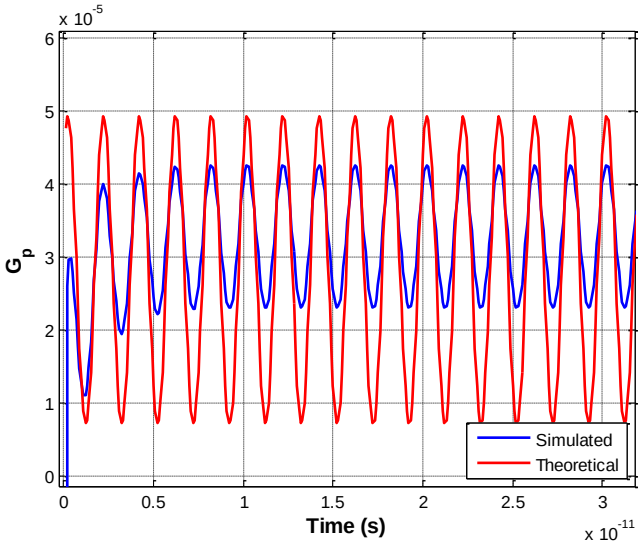

Figure 4.20 Comparision of the time-dependent conductance of the simulation model and theoritical method.

4.2.3 Photomixer Antenna Array

In the single photomixer device, the THz output power is limited by the input optical power and the bias voltage to prevent device failure. One way to improve the efficiency of the photomixer devices is to increase the active area. The THz output power can be improved by using an array of photomixers [39]. In fact, each array element is a single small-area photomixer source, and the combination of the THz beams radiating from all array elements creates a synthesized beam of an array antenna. Since there is a coherent overlap of the waves, the THz output power should be proportional to the square of the number of array elements [13]. An array of photomixers as a CW THz source has been proposed by Saeedkia et al. [44].

Considering the periodic boundary condition in the two sides of the structure, the photomixer array can be analyzed as a large photomixing structure. A cross sectional view of the single cell of photomixer array device is shown in Figure 4.21. The metal strips width is 0.4 μm and they are separated by a 1μm gap. The LTG-GaAs layer's thickness is the same as other structures (1.5 μm). The device is illuminated by two optical plane wave excitations. The total incident optical power density is 0.4 mW/μm^2, and the beat frequency is 0.5 THz. The periodic boundary condition is applied to the two sides along the x-direction of the simulation domain.

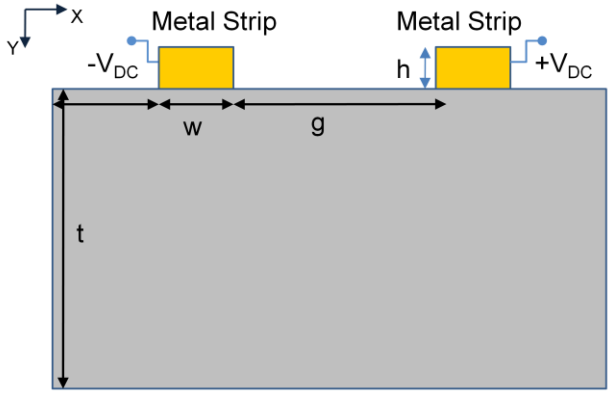

Figure 4.21 The cross sectional view of a single element of antenna array photomixer.

Figure 4.22 shows the transverse amplitude of the simulated DC photo-current versus the applied bias voltage.

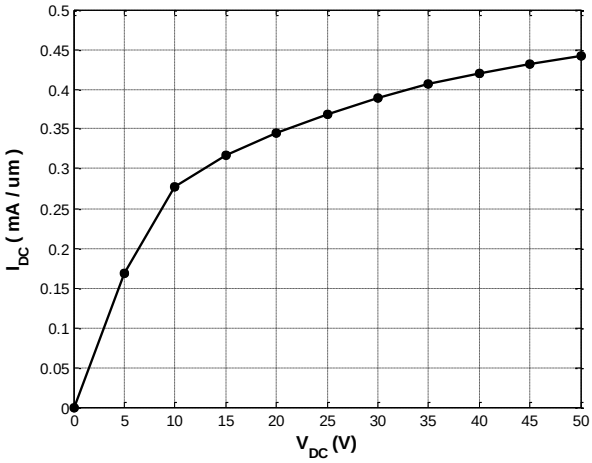

Figure 4.22 The transverse DC photo-current of photomixer.

The total incident optical power density is 0.4 mW/μm^2.

The total transverse photo-current of periodic structure versus the time is illustrated in Figure 4.23. It shows the total THz photo-current on the electrode with positive DC bias at 0.5 THz.

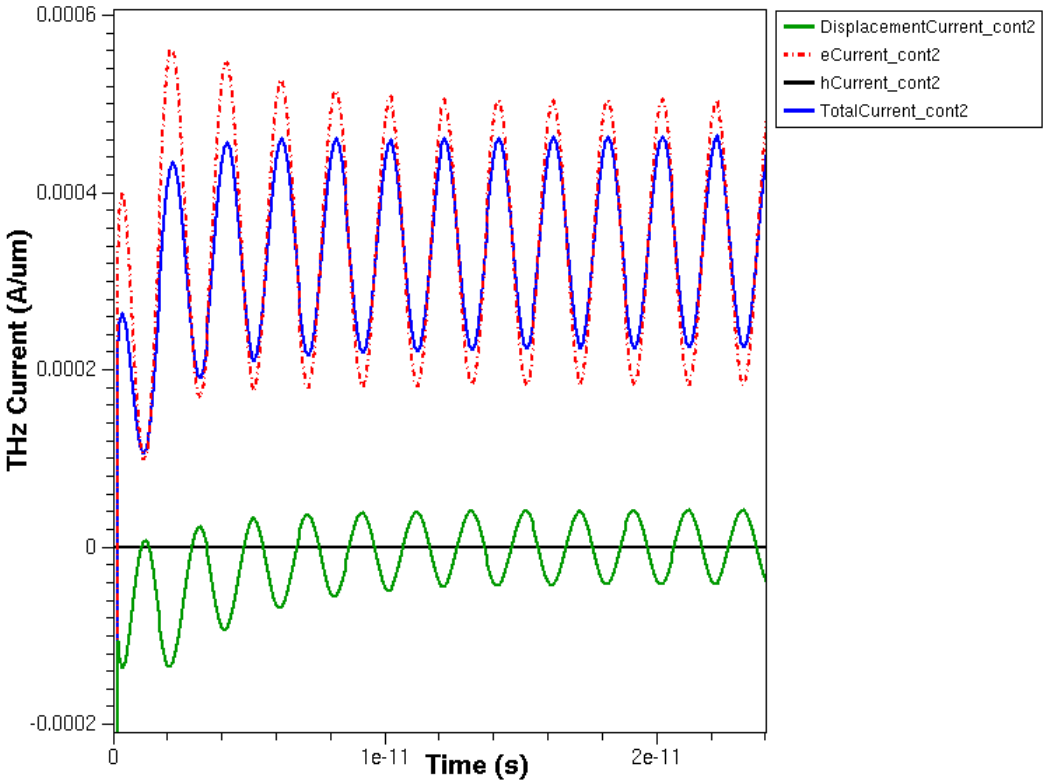

Figure 4.23 The total generated THz photo-current at the electrodes versus the time at 0.5 THz.

The total incident optical power density is 0.4 mW/μm^2.

A snapshot of the distribution of electron and hole current densities inside the LTG-GaAs layer is illustrated in Figure 4.24. The total optical power density is 0.4mW/μm^2, and the beat frequency is 0.5 THz.

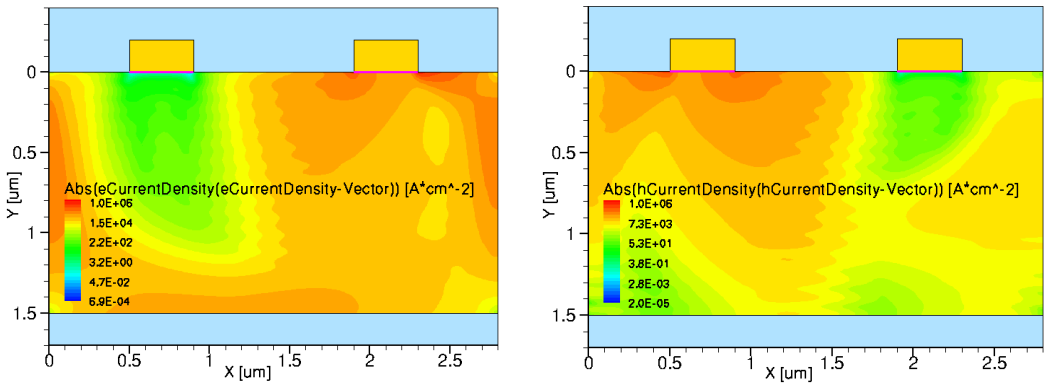

Figure 4.24 The Electron Current Density and Hole Current Density in the LTG-GaAs layer. of a periodic structure photomixer. The total optical power density is 0.4mW/μm^2, and the beat frequency is 0.5 THz.

The amplitude of the THz photo-current versus the bias voltage is shown in Figure 4.25. The total optical power density is 0.4 mW/μm^2 and the beat frequency is 0.5 THz.

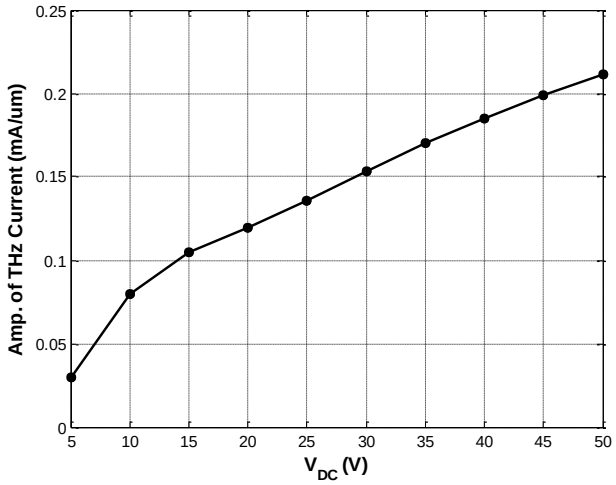

Figure 4.25 The amplitude of the THz photo-current versus the bias voltage for one element of an array photomixer.

4.3 Electromagnetic Radiation Analysis

As a current source, the photomixer drives the antenna to radiate THz waves into free space. The antenna geometry determines the input impedance of antenna. As shown from the equation (2.4), the THz output power of the photomixer is proportional to the antenna radiation resistance. The impedance of the photomixer is typically in order of 10kΩ [11] and is much higher than the impedance of the antenna integrated in the photomixer device. Therefore, an impedance mismatch is expected between the photomixer element and the antenna, which limits the THz output power. Some research works, which were briefly explained in Section 2.3.2, have been done to design antennas with high input impedance in order to improve the photomixer performance.

In this research, the computational simulation involves with two important steps; 1) current source simulation which is described in Section 4.2, and 2) the electromagnetic radiation from the antenna, which is presented in this Section. The current source is modeled by semiconductor solver in previous sections. In this section, the antenna geometry is simulated in an electromagnetic solver. Without the loss of the generality, the dipole antenna is designed at a certain frequency for THz radiations, and alternatively, the bow-tie antenna is simulated as a broadband antenna operating for a wide range of frequencies.

4.3.1 Antenna Simulation and Characterization

The dipole antenna provides higher radiation resistance at the resonance frequency in compared to broadband antennas, and consequently, increases the THz power radiations. As an example a center-feed dipole antenna is modeled. The geometry of a planar dipole antenna on LTG-GaAs substrate is illustrated in Figure 4.26. The length of dipole antenna is optimized to obtain resonant frequency at 0.5 THz. The input impedance of designed dipole antenna is depicted in Figure 4.27.

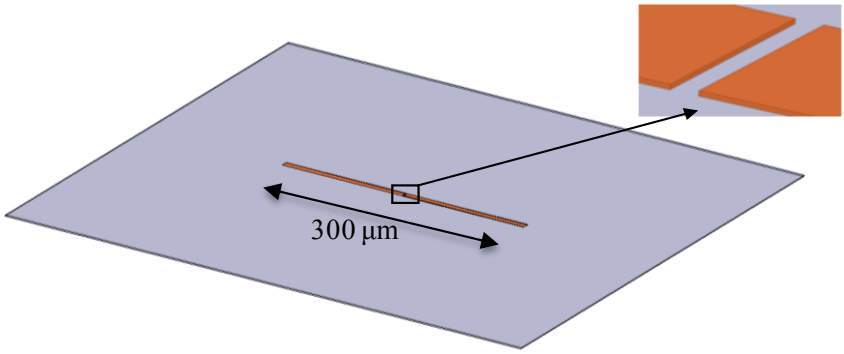

Figure 4.26 The dipole anttena geometry.

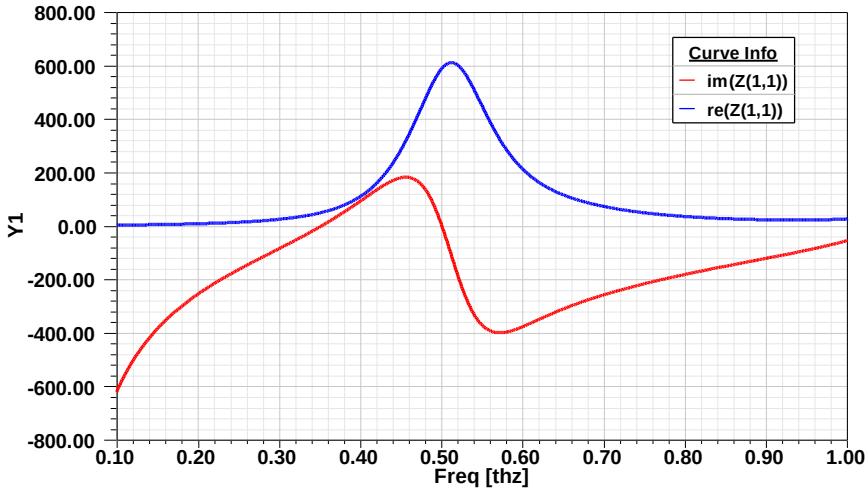

Figure 4.27 The impedance of the dipole antenna versus the beat frequency.

For broadband applications, it is of interest to have uniform THz radiated power over a wide range of frequencies. For this purpose, the broadband antennas are integrated in the photomixer device [15, 21, 26]. As an example of broadband antennas, the bow-tie antenna shown in Figure 4.28 is employed for the photomixer device. The bow-tie antenna with 1μm photoconductive gap has been designed to operate from 0.1THz to 1THz. The input impedance of the antenna is shown in Figure 4.29.

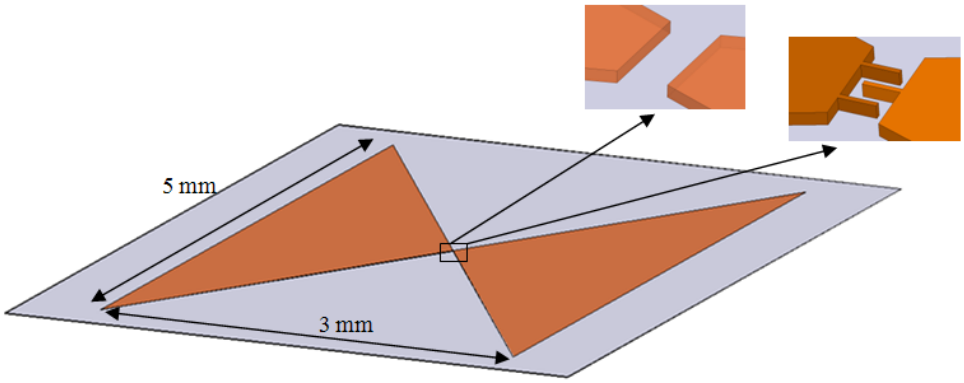

Figure 4.28 The THz anttena geometry: (a) simple photoconductive gap, and (b) interdigitated-electrodes.

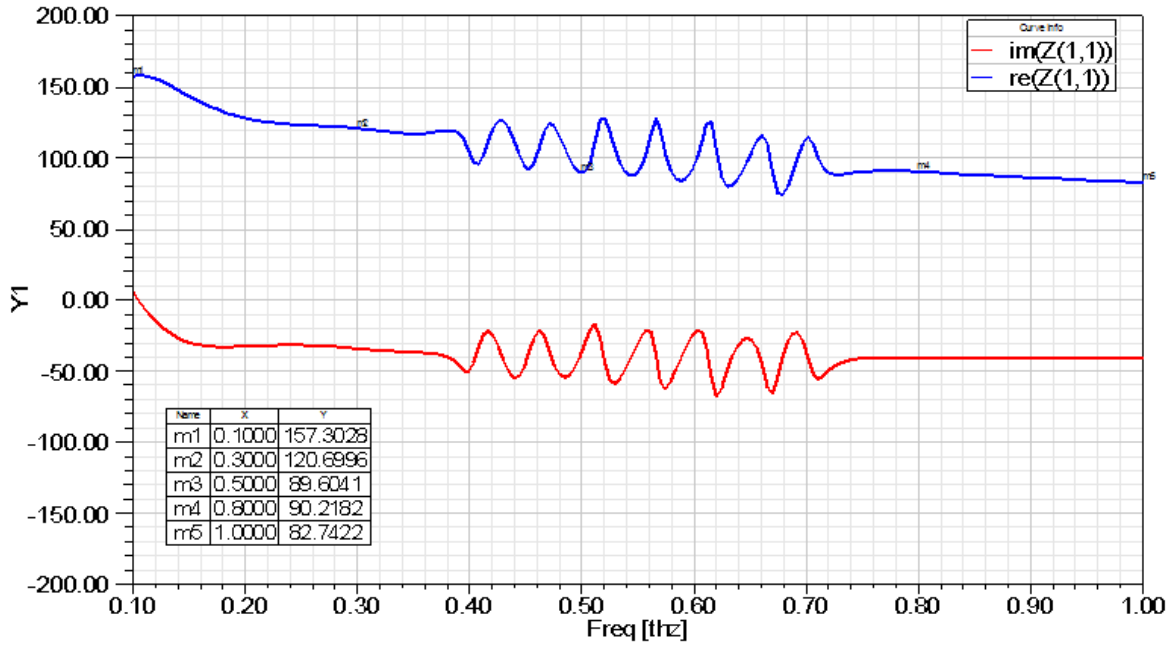

Figure 4.29 The impedance of the bow-tie antenna versus the beat frequency

The THz radiated power of the photomixer device can be obtained as [25]:

$$P_{THz} = \frac{1}{2} R_A I_{THz}^2 \tag{4.6}$$

where R_A is the radiation resistance of the antenna and I_{THz} is the generated THz photo-current in photomixer device. Calculating I_{THz} and obtaining R_A from the antenna simulation, Figure 4.30 shows the radiated power from the bow-tie and dipole antenna with 1um gap. The applied optical power density is 0.4 mW/μm^2, and the bias voltage is 20V.

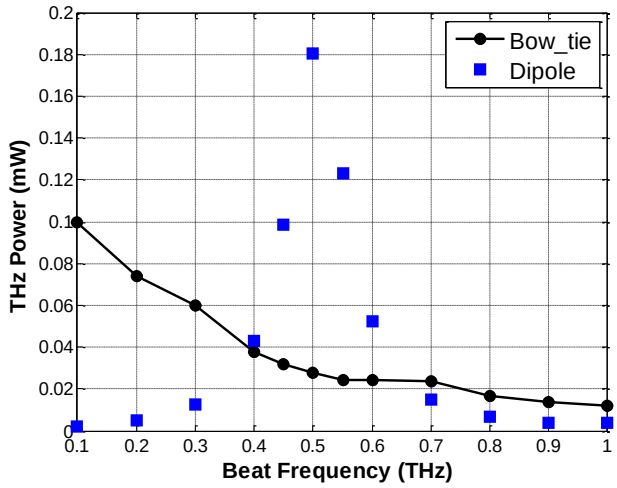

Figure 4.30 THz radiated power from the bow-tie and dipole antenna photomixer.

As can be observed in Figure 4.30, the THz radiated power is maximized at the resonant frequency (0.5 THz) of the dipole antenna. Using the broadband bow-tie antenna, the THz radiated power is more uniform for the whole range of frequencies rather than being maximized at a certain frequency as observed in the case of the dipole antenna. Obviously, if the radiation resistance of broadband antenna has less variation over the range of frequencies, more uniform THz radiated power spectrum can be obtained.

Chapter 5
Conclusion and Future Work

5.1 Conclusion

In this research, the photomixing theory and the principles of the CW THz photomixer sources were reviewed. The THz photomixer device performance is mainly limited by several factors such as the optical power coupling, the electrical field break-down, the thermal break-down, the carrier lifetime, and the RC time constants. Taking these limiting factors into account, the photomixer structure including the integrated antenna geometry and the material properties should be modeled in order to maximize the THz radiated power.

The photomixers are usually modeled by an equivalent circuit. Although the presented circuit model provides a simple explanation of the device physics and limitations, making simplistic assumptions cannot explain all aspects of the physical mechanisms inside the photomixer device. Obtaining the generated THz photo-current while considering all the important physical phenomena inside a photomixer device is an important step in the photomixer modeling. This research contributes in developing a computational simulation method to solve both semiconductor and electromagnetic problems for modeling the integrated THz photomixer Antenna devices in rigorous manner. By solving Maxwell's equations based on the FDTD method, the optical intensity distribution and consequently the optical generation rate can be obtained inside the photoconductive layer of the photomixer device. Employing the optical generation rate, the drift-diffusion partial differential equations can be solved in a semiconductor solver to achieve the generated THz photo-current inside the that region. In this research, a simple photoconductive gap photomixer, an interdigirated-electrodes photomixer, and an array structure of a photomixer were modeled and analyzed. The generated THz photo-current inside the photoconductive layer was obtained and used as a current source in the antenna feed to find the radiated THz power. The antenna structure simulation and input impedance calculations were performed by a full wave electromagnetic simulator.

Additionally, a parametric analysis was performed to observe the effects of different parameters on integrated THz photomixer antenna performance at pre-fabrication stage. The results show how the generated THz photo-current increases with higher applied optical power and DC bias voltage. However, the maximum THz photo-current is limited by the maximum applied optical power and DC bias voltage to avoid the device failure. The different size of photoconductive gap effect is also

studied and the simulation results show that selecting the optimum gap size is a trade-off between the photoconductive gain, the RC roll-off, and the heat dissipation. In photomixer structure, the carrier lifetime of the photoconductive material should be sub-picoseconds to obtain ultrafast THz current modulation. However, it can be observed from the simulation results that there is an optimized carrier lifetime in LTG-GaAs to achieve the maximum THz photo-current. The presented parameter analysis helps to investigate the limitations and nonlinearity effects on the photomixer device.

5.2 Future work

The following directions are suggested as future work for this research:

- The modeled CW THz photomixer devices can be fabricated and tested. The experimental results can be used to verify the simulation results for the practical applications.
- The proposed simulation strategy can be extended to more complex integrated THz active and passive structures.
- The broadband antennas can designed and optimized to provide higher radiation resistance at higher frequencies in order to obtain a uniform THz power spectrum.

Appendix A
TCAD Sentaurus Device

A.1 Introduction to TCAD Sentaurus

Sentaurus Device is one of a comprehensive set of core Synopsys TCAD products for the 1D, 2D, and 3D process, device, and system simulations. Sentaurus Device is capable of simulating the electrical, optical and thermal characteristics of a wide range of semiconductor devices. It contains state-of-the-art numeric solvers and a complete set of models for carrier and heat transport, quantization effects and heterostructures. Sentaurus Device supports the Opto and EMW modules to simulate optoelectronic devices. The Opto option enables the simulation of inactive devices with an advanced band structure and gain calculations. In addition, the EMW option implies full-wave solutions of the Maxwell's equations to account for the physical optics in advanced devices.

In Sentaurus Device, there are various methods as optical solvers to compute optical generation rate for devices with optical excitations. The following is the list of the optical solvers that Sentaurus Device supports [40]:

- *RayTracing* (RT)Method
- *Transfer Matrix Method* (TMM)
- *Finite-difference time-domain* (FDTD) Method
- *Beam Propagation Method* (BPM)

In semiconductor devices, the physical phenomena are very complex. Based on the applications, they can be expressed by partial differential equations with different level of difficulty. Sentaurus Device allows for arbitrary combinations of transport equations and physical models to simulate and analyze all kinds of semiconductor devices.

Sentaurus Device directly interfaces with Sentaurus Process and Sentaurus Structure Editor for generating device structures and with Sentaurus Workbench for visualizing and controlling the simulation projects. Eventually the Inspect and Tecplot_SV programs were used for visualizing and analyzing the Sentaurus Device results.

Some significant advantages of Sentaurus Device are listed as below [40]:

- Capable of handling arbitrary geometries in 1D, 2D, and 3D

- Includes a complete set of analysis modes: DC, transient, AC, and harmonic balance
- Explores the new device ideas while they aren't fabricated yet
- Characterizes the electrical, optical and thermal behavior of semiconductor devices for fast prototyping, development and optimization

The following sections briefly introduce the Sentaurus Device tools.

A.1.1Sentaurus Workbench

Sentaurus Workbench is a graphical interface for creating, controlling, implementing and analyzing TCAD simulations. In fact, this framework tool allows the user to manage the information flow, including the preprocessing of the user input files, the parameterize projects, the set up and implement tool instances, and the visualize results [40]. Sentaurus Workbench contains a command and mask layout interface to create, edit, and organize process flow. It is known as a project control tool in TCAD Sentaurus.

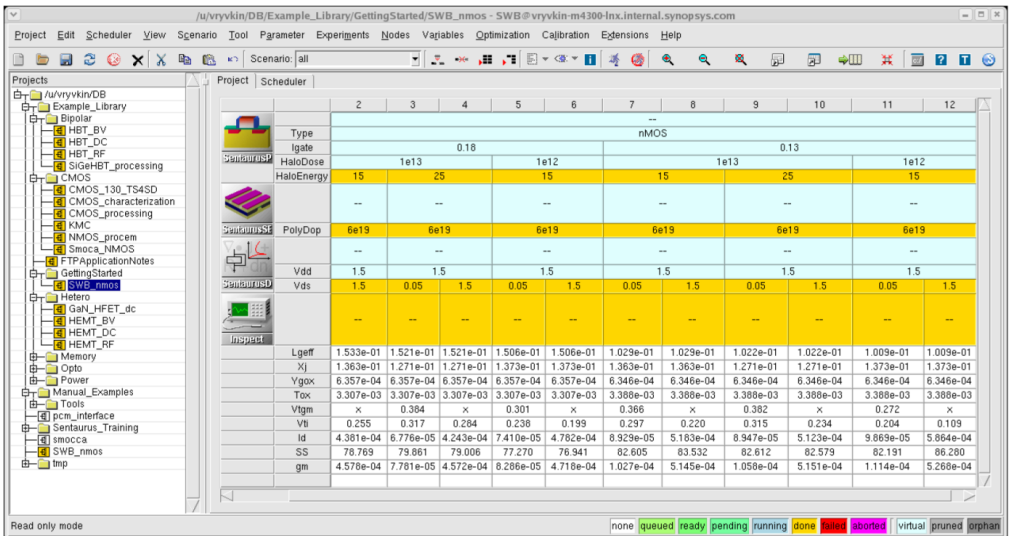

Figure A.1 Project Editor main view [40].

The Figure A.1 shows a Graphical User Interface (GUI) of the project editor in Sentaurus Workbench. This GUI provides the opportunity to access, organize and edit a database of the projects. As it can be seen in Figure A.1, there are some toolbars for browsing the projects, setting and controlling the simulations.

A.1.2 Sentaurus Process

Sentaurus Process is an advanced multidimensional process simulator for developing and optimizing silicon and non-silicon technologies. Sentaurus Process provides a predictive framework to simulate a broad spectrum of technologies.

A.1.3 Sentaurus Structure Editor

Sentaurus Structure Editor can be used as a 2D or 3D structure editor, and a 3D process emulator to create TCAD devices. In Sentaurus Structure Editor, the structures can be generated and edited by using GUI or scripts. The doping and meshing of the structure can be defined interactively. Furthermore, it generates the required input files like the mesh command file and the TDR boundary file for meshing engines which generate the TDR grid and the data file for the device structure [40].

The GUI of Sentaurus Structure Editor has three main work areas which can be seen in Figure A.2.

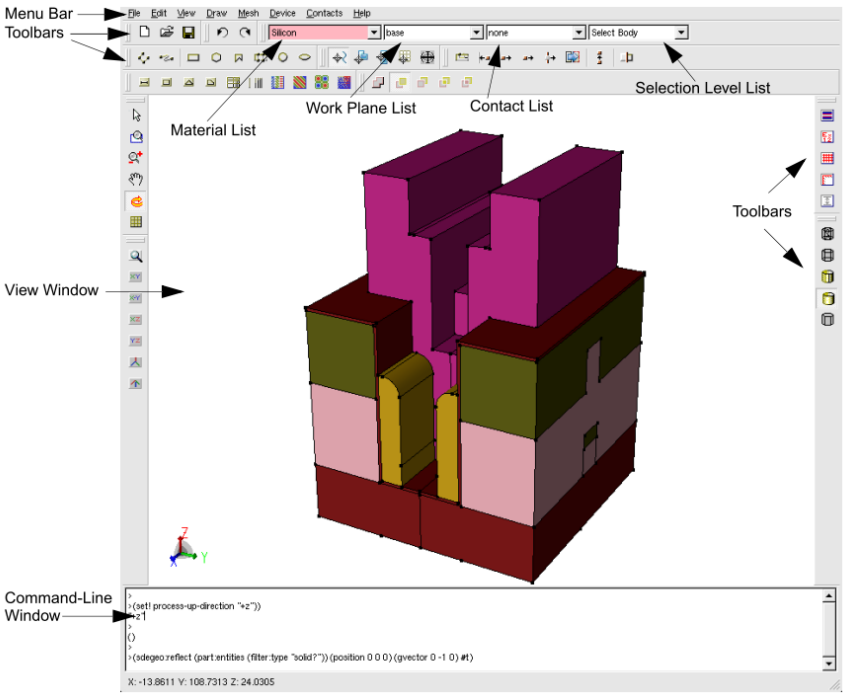

Figure A.2 Main window of Sentaurus Structure Editor [40].

For defining a 2D or 3D device structure in GUI of Sentaurus Structure Editor, the following steps should be done:

- Generate the model geometry.

- Define the contact regions in the model.
- Add the constant, the analytic, and the externally generated doping profiles to the model.
- Define the local refinements.
- Include the external sub meshes.
- Interface to the Synopsys meshing engines.

A.1.4 Inspect

Inspect is one of TCAD Sentaurus tools for showing and analyzing the simulation results. It has a GUI, a script language, and an interactive language for computations with curves. Inspect can read various data and file formats such as TXT, TDR, TIF, DF_ISE, CSV, XGRAPG, and XMGR [40]. Figure A.3 shows the GUI of Inspect which consists of a few toolbar and work areas.

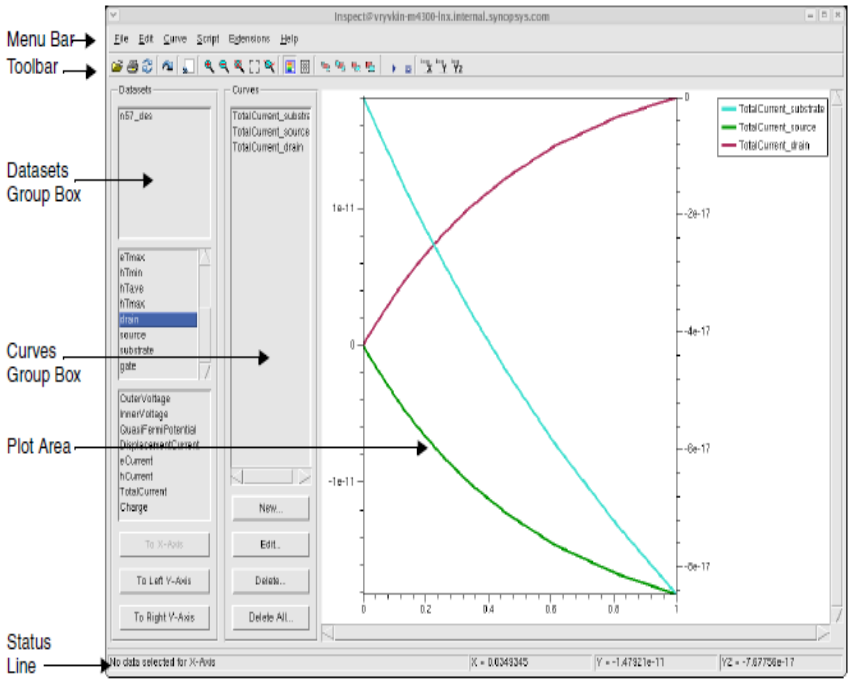

Figure A.3 Main window of Inspect [40].

Inspect can show the graphs from Sentaurus Device simulation results in *.plt format. Those graphs can contain the voltage, the current etc, the time or each pair of datasets.

A.1.5 Tecplot_SV

Tecplot is a general purpose package for viewing 2D and 3D plots. The complete package of the Tecplot, Synopsys TCAD add on and the Synopsys tecplot_sv launcher is called Tecplot_SV.

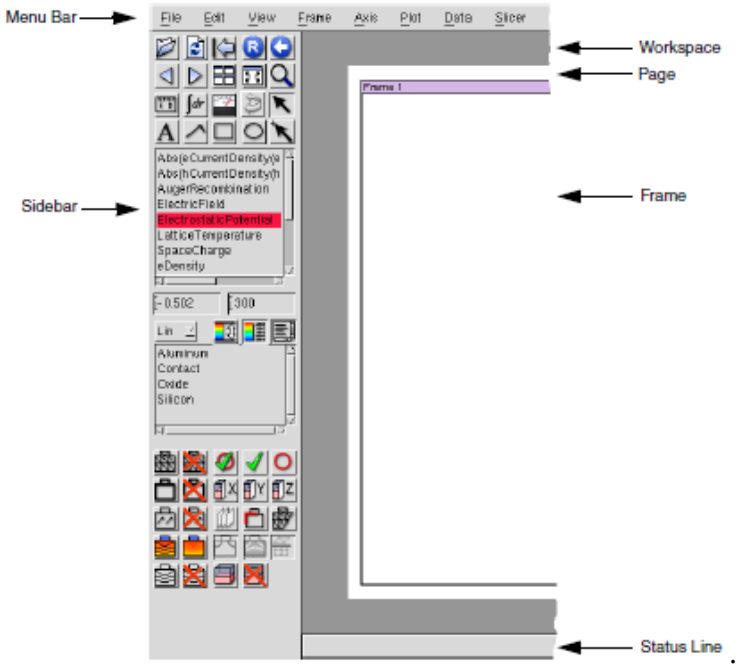

Figure A.4 Main window of Tecplot area [40].

The main Tecplot window which consists of the Synopsys menu bar and sidebar, the status line, and the Tecplot workspace is shown in Figure A.4. Tecplot_SV can read *.dat and *.grd files [40]. It can show meshes, contour plots, vectors and field distributions and so forth produced by Sentaurus Device.

A.2 Simulation Procedures of Optoelectronic Device in TCAD Sentaurus

This section demonstrates the use of TCAD Sentaurus tools for designing an optoelectronic device (CW THz photomixer). For analyzing optoelectronic devices, Sentaurus Structure Editor is used to design the device structure. Thereafter, the designed device is simulated by Sentaurus Device for the electrical, thermal and optical characterizations. Finally, the results can be displayed and analyzed by Inspect and Tecplot_SV.

The system requirements for working with this software are licensed access to TCAD Sentaurus and UNIX or an equivalent work station. It should be mentioned that the TCAD Sentaurus version C-2009.06 was used for this application.

For detailed descriptions of TCAD Sentaurus, refer to the related user manuals, various application examples and training documents provided by Synopsys.

The block diagram shown in Figure A.5 gives a big picture of how TCAD Sentaurus software works. It helps to follow the procedure in the software.

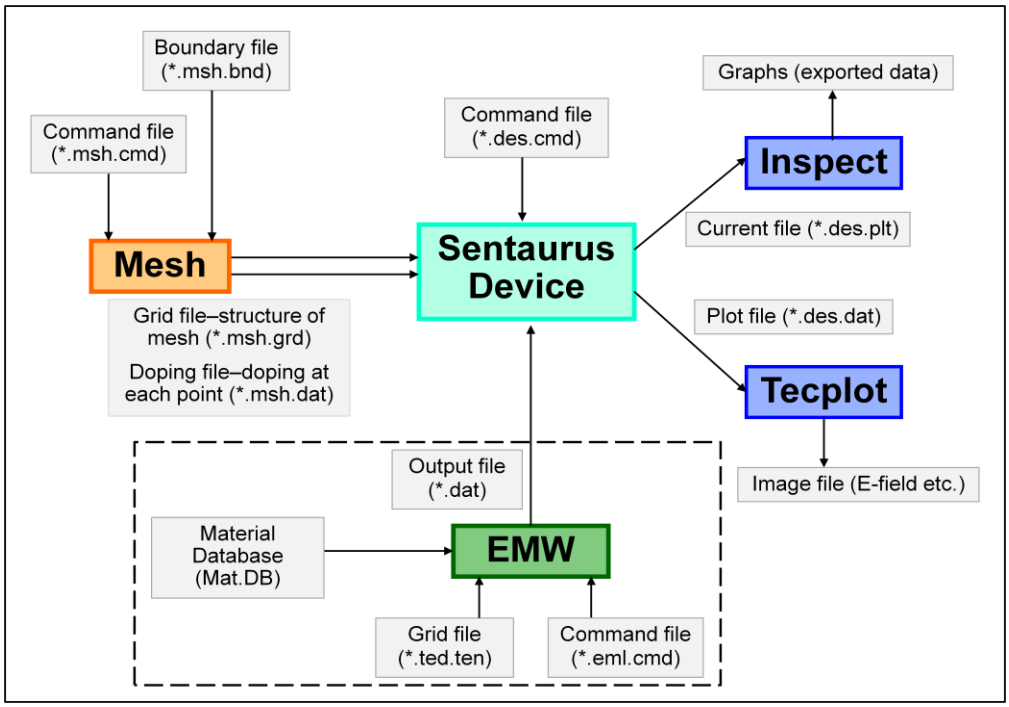

Figure A.5 A block diagram of simulation flow in Sentaurus.

The following steps explain the procedure of implementing an optoelectronic device project in TCAD Sentaurus software.

A.2.1 Building the device structure

The Sentaurus Structure Editor is used to design the device. To start Sentaurus Structure Editor, enter sde in the UNIX command line. The GUI of Sentaurus Structure Editor which can be seen in Figure A.2 will be opened. For creating a new 2D or 3D structure, the drawing toolbars or the scripts can be used. The material types, doping, contacts, and refinement regions should be specified for a defined geometry. Then the geometry is discretized into a mesh. TCAD Sentaurus supports three different

mesh engines which can be chosen depending on the application. During the design some input files which include the geometry, doping, boundary, mesh etc will be generated. These files are needed as input for doing the simulation in Sentaurus Device.

The Figure A.6 shows a 2D structure of a CW THz Photomixer device in Sentaurs Structure Editor. The device geometry, material types, device contacts, and other device information can be seen in Figure A.6.

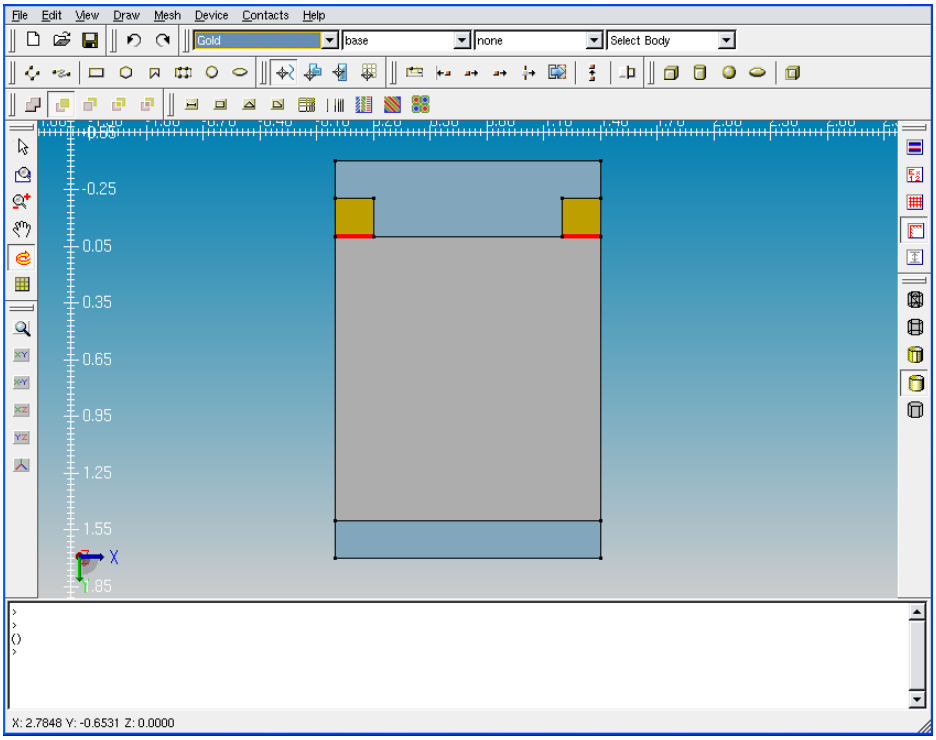

Figure A.6 Example of 2D Photomixer device structure.

A.2.2 Running the device simulation

To simulate a device, the Sentaurus Device simulator requires an input command file which is a text file (*_des.cmd format) including the required commands and parameters for the simulation. There are the mandatory sections for a typical input command file. The command file specifies the following:

- File: Contains the input and output files.
- Electrode: Contains list of the contacts and bias voltages.

- Physics: Contains physical models used in the simulation.
- Plot and CurrentPlot: Contains the variables included in the output files.
- Math: Controls the solve section
- Solve: Contains the simulation conditions and equations.

In general, the Sentaurus Device simulator takes mesh, applies the semiconductor equations and boundary conditions and then solves.

Senaurus Device supports four different carrier transport models. Depending on the device under investigation and the required accuracy, one of them can be chosen. The carrier transport models in the semiconductor device are drift-diffusion, Hydrodynamic, Thermodynamic and Monte Carlo. For the photomixer application, the drift-diffusion carrier transport model is preferred. The set of basic drift-diffusion equations in the time domain consists of Poisson's equation, continuity equations, and current equations for electrons and holes.

One of the significant advantages of the Sentaurus Device for photomixer application is that any number of excitations can be used as device sources. Also all the different types of excitation can be mixed in a model.

Sentaurus Devicre Electromagnetic Wave (EMW) Solver

The EMW solver is an optional module in Sentaurus, which improves capabilities of the Sentaurus device for simulating optoelectronic devices. The EMW option allows full-wave solutions of the Maxwell's equations to account for the physical optics in advanced devices. The EMW solver requires a command file (*_eml.cmd format) with mandatory sections to do electromagnetic simulations [40]. The EMW command file specifies the following:

- Globals: Specifies global simulation parameters.
- Boundary: Selects boundary conditions.
- Excitation: Specifies the source of the electromagnetic field.
- Sensor: Sets up a sensor for tracing integral quantities.
- Plot: Defines a plot for visualization or data exchange.

- Extractor: Computes higher level quantities based on the input from sensors or directly from the grid values.
- Detector: Automatic, conditional termination of a simulation.

The output result of the EMW can be loaded into the Sentaurus Device simulator as an input file. In the photomixer application, the input file of the device simulator is an optical generation rate (EMW solver output). The computational methods in the EMW solver are the *Finite Difference Time Domain* (FDTD) which is the default method, the *Transfer Matrix Method* (TMM), *Ray Tracing* (RT), and the *Beam Propagation Method* (BPM). Depending on the application, each of the methods can be selected. The photomixer device should be analyzed in the time domain. Therefore, in this application, the FDTD method is used to solve Maxwell's equations.

A.2.3 Visualizing the Output Results

Tecplot_SV is one of TCAD Sentaurus tools for viewing the 2D and 3D simulation results. The files which can be loaded with Tecplot_SV are *.dat and *.grd formats [40]. The variables such as the field distribution, mesh, optical generation and so forth which are listed in the sidebar can be plotted as simulation results. To start the Tecplot_SV, enter tecplot_sv in the UNIX command line.

Inspect is a TCAD Sentaurus tool for plotting 1D graphs of the simulation results. It can read *.plt formats and plots each pair of datasets. All the simulation results can be exported in different formats. Therefore the results can be used and analyzed using other softwares. To start the Inspect, enter inspect in the UNIX command line.

Appendix B
Sentaurus Command files

A. EMW Command File

The following command file is an example of the EMW command file which was used for a 2D MSM photomixer project.

```
Preprocess {
    Mode = BoundaryToGrid
    Input = 2d_pm_1um_new0.bnd
    Output = 2d_pm_1um_new0_ted.ten
    CellsPerWavelength = 20
    Wavelength = 0.8e-6
    }
Globals {
    GridFile = 2d_pm_1um_new0_ted.ten
    Polarization = TM
    TotalSimulationTime = 4e-12
    }
Boundary {
    Sides = {X Y}
    Type = mur
    }
Excitation {
    Type = Scattering
    IncidentField = Planewave
    Region = automatic
    Signal = linsin
```

Theta = 180

Frequency = 3.75e14

NRise = 5

Amplitude = 388325.18

}

Excitation {

Type = Scattering

IncidentField = Planewave

Region = automatic

Signal = linsin

Theta = 180

Frequency = 3.755e14

NRise = 5

Amplitude = 388325.18

}

Extractor {

Type = OpticalGeneration

Name = n1_1um_05thz_I04

Region = {sub gold1 gold2 air_lump_1 air_lump_2}

DfgeoFile = 2d_pm_1um_new0_msh.grd

}

Plot {

Quantity = {AbsElectricField ElectricField}

Type = dfgeo

Name = Efield_1um_05thz_I04

Region = {sub gold1 gold2 air_lump_1 air_lump_2}

DfgeoFile = 2d_pm_1um_new0_msh.grd

OutputFormat = ASCII

TickStep = 100000

}

Sensor {

Region = sensor_E1

Name = sensor_E1_1um_05thz_I04

Type = ComponentE

}

Run {

FlushStep = 500

ScreenCounterStep = 500

}

B. Sdevice Command File

The following command file is an example of the input file for the device simulation:

Electrode {

{ Name="cont1" Voltage= 0}

{ Name="cont2" Voltage= 20}

}

File {

Grid = "2d_pm_1um_new0_msh.grd"

Doping = "2d_pm_1um_new0_msh.dat"

OpticalGenerationInput = "n1_1um_05thz_I04_generation_eml.dat"

OptGenTransientScaling = "time_16p.txt"

Parameter = "models.par"

Save = "n2_1um_05thz_20v_16p_I04"

Current = "n2_1um_05thz_20v_16p_I04"

Output = "n2_1um_05thz_20v_16p_I04"

}

Plot {

Doping

eDensity hDensity

eLifetime hLifetime

Potential

ElectricField/Vector

Current/Vector

ConductionCurrent/Vector

eCurrent/Vector hCurrent/Vector

DisplacementCurrent/Vector

eMobility hMobility

TotalRecombination

SRHRecombination

OpticalField

}

CurrentPlot {

ElectricField ((0.1 -0.1) (1.3 -0.1) (0.2001 -0.01) (1.199 -0.01) (0.201 -0.01) (1.19 -0.01) (0.201 -0.1) (1.19 -0.1) (0.201 -0.2) (1.19 -0.2) (1.1 -0.01) (1.1 -0.1) (1.1 -0.2))

ElectricField/Vector ((0.1 -0.1) (1.3 -0.1) (0.2001 -0.01) (1.199 -0.01) (0.201 -0.01) (1.19 -0.01) (0.201 -0.1) (1.19 -0.1) (0.201 -0.2) (1.19 -0.2) (1.1 -0.01) (1.1 -0.1) (1.1 -0.2))

Potential ((0.1 -0.1) (1.3 -0.1) (0.2001 -0.01) (1.199 -0.01) (0.201 -0.01) (1.19 -0.01) (0.201 -0.1) (1.19 -0.1) (0.201 -0.2) (1.19 -0.2) (1.1 -0.01) (1.1 -0.1) (1.1 -0.2))

}

```
Physics {
        Optics (
                OpticalGeneration (
                        ReadFromFile(
                        TimeDependence (FromFile)
                                )  )
                )
        EffectiveIntrinsicDensity ( OldSlotboom NoFermi )
        Mobility( DopingDep )
        Recombination ( SRH(DopingDependence) Auger)
        }
Math {
        Extrapolate
        RelErrControl
        Digits=5
        ErrRef(electron)=1.e10
        ErrRef(hole)=1.e10
        Iterations=10
        transient=BE
}
Solve {
        Transient ( InitialTime= 0
        FinalTime = 32e-12
        InitialStep = 0
        MaxStep = 1e-13
        MinStep = 1e-14)
```

```
{ coupled (Iterations=10) {poisson electron hole}

Plot ( Fileprefix = "n2_1um_05thz_20v_16p_I04_snapshot"

        Time = (0.25e-12; 0.5e-12; 0.75e-12; 1e-12; 16e-12; 19e-12; 20e-12; 32e-12 )

        NoOverwrite)

}

Plot (Fileprefix= "n2_1um_05thz_20v_16p_I04_s"){}

Save (Fileprefix= "n2_1um_05thz_20v_16p_I04_s"){}

}
```

Bibliography

[1] M. Nagel, M. Först, and H. Kurz, "THz biosensing devices: fundamentals and technology," *Journal of Physics: Condens. Matter*, vol 18, pp. 601–618, 2006.

[2] S. M. Kim, F. Hatami, and J. S. Harris, "Biomedical THz imaging with a quantum cascade laser," *Applied Physics Letters*, vol. 88, 153903, 2006

[3] P. F. Taday, "Applications of THz spectroscopy to pharmaceutical sciences," *Phil. Trans. R. Soc. A*, vol. 362, no. 1815, pp. 351–364, 2004.

[4] V. P. Wallace, P. F. Taday, A. J. Fitzgerald, R. M. Woodward, J. Cluff, R. J. Pye, and D. D. Arnone, "THz pulsed imaging and spectroscopy for biomedical and pharmaceutical applications ," *Faraday Discuss.*, vol. 126, pp.255–263, 2004.

[5] C. Baker, W. R. Tribe, T. Lo, B. E. Cole, S. Chandler, and M. C. Kemp, "People screening using THz technology", *Proceedings of SPIE*, vol.5790, pp. 1–10, 2005.

[6] R. Piesiewicz, J. Jemaia, M. Kochb, T. Krnera, "THz channel characterization for future wireless gigabit indoor communication systems," *Proceedings of SPIE*, vol. 5727, pp. 166–176, 2005.

[7] A. Rudolph, J. Simpson, M. Haas, E. Erickson, and M. Fich, "Far-infrared abundance measurements in the outer galaxy," *Astrophysical Journal*, vol. 489, pp. 94-101, 1997.

[8] M. Wiedner, et al., "First observations with CONDOR, a 1.5 THz heterodyne receiver," *Astronomy & Astrophysics*, vol. 454, pp. L33–L36, 2006.

[9] R. M. Woodward, V. P. Wallace, R. J. Pyle, B. E. Cole, D. D. Arnone, E. H. Linfield, and M. Pepper, "THz pulse imaging of ex vivo basal cell carcinoma," *Journal of Investigative Dermatology*, vol. 120, no. 1, pp. 72–78, 2003.

[10] D. Crawley, C. Longbottom, V. P. Wallace, B. E. Cole, D. D. Arnone, and M. Pepper, "Three-dimensional THz pulse imaging of dental tissue," Journal of Biomedical Optics, vol. 8, pp. 303–307, 2003.

[11] S. M. Duffy, S. Verghese, K. A. McIntosh, A. Jackson, A. C. Gossard, and S. Matsuura, "Accurate modeling of dual dipole and slot elements used with photomixers for coherent THz output power*," IEEE Trans. Microw. Theory Tech.*, vol. 49, no. 6, pp. 1032–1038, 2001.

[12] D. Saeedkia and S. Safavi-Naeini, "THz Photonics: Optoelectronic Techniques for Generation and Detection of THz Waves," *Journal of Lightwave Technology*, vol. 26, no. 15, 2008.

[13] S. Matsuura and H. Ito, "Generation of CW THz Radiation with Photomixing," *Topics in Applied Physics*, vol. 97, Springer-Verlag Berlin, pp. 157–202, 2005.

[14] E. R. Brown, F. W. Smith, and K. A. McIntosh, "Coherent millimeter-wave generation by heterodyne conversion in low-temperature-grown GaAs photoconductors," *Journal of Applied Physics*, vol. 73, 3, pp. 1480–1484, 1993.

[15] E. R. Brown, K. A. McIntosh, K. B. Nichols, and C. L. Dennis, "Photomixing up to 3.8 THz in low-temperature-grown GaAs," *Applied Physics Letters*, vol. 66, 3, pp. 285–287, 1995.

[16] S. Matsuura, M. Tani, and K. Sakai, Generation of coherent THz radiation by photomixing in dipole photoconductive antennas, *Applied Physics Letters*, vol. 70, 5, pp. 559–561 1997.

[17] I. S. Gregory, H. Page and L. Spencer, "Continuous-Wave THz Photomixer Systems for Real-World Applications," *THz Frequency Detection and Identification of Materials and Objects* Edited by R.E. Miles et al., pp. 167–184, Springer, 2007.

[18] S. Verghese, K. A. McIntosh, S. Calawa, W. F. Dinatale, E. K. Duerr, and K. A. Molvar, "Generation and detection of coherent THz waves using two photomixers", *Applied Physics Letters*, vol. 73, 26, pp. 3824–3826, 1998.

[19] D. Saeedkia and S. Safavi-Naeini, "A Comprehensive Model for Photomixing in Ultrafast Photoconductors," *IEEE Photonics Technology. Letters*, vol. 18, no. 13, pp. 1457–1459, 2006.

[20] E. R. Brown, "THz generation by photomixing in ultrafast photoconductors," *Int. J. High Speed Electron. Syst.*, vol. 13, no. 2, pp. 497–545, 2003.

[21] I. S. Gregory, C. Baker, W. R. Tribe, I. V. Bradley, M. J. Evans, E. H. Linfield, A. G. Davies, and M. Missous, "Optimization of Photomixers and Antennas for Continuous-Wave THz Emission," *IEEE J. Quantum Elec.*, vol. 41, no. 5, pp. 717–728, 2005.

[22] M. Tani, O. Morikawa, S. Matsuura and M. Hangyo, "Generation of THz radiation by photomixing with dual- and multiple-mode lasers," *Semicond. Sci. Technol.*, vol. 20, pp. 151–163, 2005.

[23] M. Tani, P. Gu, M. Hyodo, K. Sakai, and T. Hidaka, "Generation of coherent THz radiation by photomixing of dual-mode lasers," *Opt. Quantum Electron.*, vol. 32, pp. 503–520, 2000.

[24] C. Kadow, S.B. Fleischer, J.P. Ibbetson, J.E. Bowers, A.C. Gossard, J.W. Dong, and C.J.Palmstrom, *Applied Physics Letters*, vol. 75, pp. 3548, 1999.

[25] S. Preu, G. H. Dohler, S. Malzer, L. J. Wang, and A. C. Gossard, "Tunable, continuous-wave THz photomixer sources and applications," *Journal of Applied Physics*, vol. 109,pp. 061301, 2011.

[26] S. Verghese, K. A. McIntosh and E. R. Brown, "Highly tunable fiber coupled photomixers with coherent THz output power," *IEEE Trans. Microw. Theory Tech.*, vol. 45, pp. 1301–9, 1997.

[27] S. M. Duffy, S. Verghese, K. A. McIntosh, A. Jackson, C. Gossard, and S. Matsuura, "Accurate Modeling of Dual Dipole and Slot Elements Used with Photomixers for Coherent THz Output Power," *IEEE Trans. Microwave Theory Tech.*, vol. 49, no. 6, pp. 1032–1038, 2001.

[28] S. Matsuura, G. A. Blake, R. A. Wyss, J. C. Pearson, C. Kadow, A. W. Jackson, and A. C. Gossard, "A traveling-wave THz photomixer based on angle-tuned phase matching," *Applied Physics Letters*, vol. 74, no. 19, pp. 2872–2874, 1999.

[29] E. R. Brown, "A photoconductive model for superior GaAs THz photomixers," *Applied Physics Letters*, vol. 75, pp. 769–71, 1999.

[30] M. Neshat, D. Saeedkia, L. Rezaee and S. Safavi Naeini, "A Global Approach for Modeling and Analysis of Edge-Coupled Traveling-Wave THz Photoconductive Sources," *IEEE trans. Microwave Theory Tech.*, vol. 58, no. 7, 2010.

[31] S. Selberherr, *Analysis and Simulation of Semiconductor Devices*, Wien, Austria: Springer-Verlag, 1984

[32] G. Carelli, D. Pereira, and F. Strumia, "Hetrodyne Frequency MeasuremntS of FIR Laser Lines around 1.2 and 1.4 THz," *IEEE J. Quantum Electron.*, vol. 31, 144, 1995.

[33] A. S. Pine, R. D. Suenram, E. R. Brown, and K. A. McIntosh, "A THz Photomixing Spectrometer: Application to SO2 Self Broadening," *J. Mol. Spectrosc.*, vol. 175, pp. 37–47, 1996.

[34] D. M. Mittleman, R. H. Jacobsen, R. Neelamani, R. G. Baraniuk, and M. C. Nuss, "Gas sensing using THz time-domain spectroscopy," *Appl. Phys. B*, vol. 67, pp. 379, 1998.

[35] I. S. Gregory, W. R. Tribe, C. Baker, B. E. Cole, M. J. Evans, L. Spencer, M. Pepper, and M. Missous, "Continuous-wave THz system with a 60 dB dynamic range," *Applied Physics Letters*, vol. 86, pp. 204104, 2005.

[36] K. J. Siebert, T. Löffler, H. Quast, M. Thomson, T. Bauer, R. Leonhardt, C. Czasch, and H. G. Roskos, "All-optoelectronic continuous wave THz imaging for biomedical applications," *Physics in Medicine and Biology*, vol. 47, pp. 3743–3748, 2002.

[37] S. M. Sze, *Physics of Semiconductor Devices*, New York: John Wiley & Sons, 2nd edition, 1981.

[38] M Neshat, "Theory, Design and Development of Resonance Based Biosensors in THz and Millimeter-wave,"Ph.D. dissertation, Dept. Elect. Comput. Eng., Univ. Waterloo, Waterloo, ON, Canada, 2009.

[39] D. Saeedkia, "Modeling and design of photoconductive and superconductive THz photomixer sources," Ph.D. dissertation, Dept. Elect. Comput. Eng., Univ. Waterloo, Waterloo, ON, Canada, 2005.

[40] TCAD Sentaurus. Synopsys. [Online]. Available: http://www.synopsys.com

[41] E. Palm and F. Van de Wiele, "Current Lines and Accurate Contact Current Evaluation in 2D Numerical Simulation of Semiconductor Devices," *IEEE Transactions on Electron Devices*, vol. ED. 32, no. 10, pp. 2052–2059, 1985.

[42] M. C. Teich, "Field-Theoretical Treatment of Photomixing," *Applied Physics Letters*, vol. 14, no. 6, pp. 201–203, 1969.

[43] E. R. Brown, K. A. McIntosh, F. W. Smith, K. B. Nichols, M. J. Manfra et al. "Milliwatt output levels and superquadratic bias dependence in a low-temperature-grown GaAs photomixer," *Applied Physics Letters*, vol. 64, no. 24, pp. 3311–3313, 1994.

[44] D. Saeedkia, R. R. Mansour, and S. Safavi-Naeini, "Analysis and Design of a Continuous-Wave THz Photoconductive Photomixer Array Source," *IEEE Trans. Antennas Propag.*, vol. 53, no. 12, pp. 4044–4050, 2005.

[45] E. Rouvalis, C. C. Renaud, D. G. Moodie, M. J. Robertson, and A. J. Seeds, "Traveling-Wave Uni-Traveling Carrier Photodiodes for CW THz Generation," *Opt. Express*, 18, 11105, 2010.

[46] E. Peytavit, A. Beck, T. Akalin, J.-F. Lampin, F. Hindle, C. Yang, and G. Mouret, "Continuous terahertz-wave generation using a monolithically integrated horn antenna," *Applied Physics Letter*, 93, 111108, 2008.